**Article**

# Tipping point-induced abrupt shifts in East Asian hydroclimate since the Last Glacial Maximum

Fuzhi Lu [1], Huayu Lu [1] ✉, Yao Gu[1], Pengyu Lin [1], Zhengyao Lu [2], Qiong Zhang [3], Hongyan Zhang [1], Fan Yang[1], Xiaoyi Dong[1], Shuangwen Yi[1], Deliang Chen [4], Francesco S. R. Pausata [5], Maya Ben-Yami [6,7] & Jennifer V. Mecking [8]

Multiple tipping points in the Earth system could be triggered when global warming exceeds specific thresholds. However, the degree of their impact on the East Asian hydroclimate remains uncertain due to the lack of quantitative rainfall records. Here we present an ensemble reconstruction of East Asian summer monsoon (EASM) rainfall since the Last Glacial Maximum (LGM) using nine statistical and machine learning methods based on multi-proxy records from a maar lake in southern China. Our results define five tipping points in the EASM rainfall since the LGM, which are characterized by abrupt and irreversible regime shifts with a median amplitude of 387 ± 73 mm (24 ± 5 %). Combined with multi-model simulations and existing records, we attribute these tipping points to cascades of abrupt shifts in the Atlantic meridional overturning circulation (AMOC) and Saharan vegetation. Our findings underscore the nonlinear behavior of the EASM and its coupling with other tipping elements.

The tipping point is a critical threshold beyond which a small perturbation can qualitatively transform the state or evolution of a system[1]. A climate tipping point happens when a minor variation in forcing triggers a profound nonlinear response in the dynamic processes within the climate system, leading to an abrupt and irreversible regime shift[2]. There has been increasing awareness and concern that global warming could trigger tipping points in the climate system, introducing far-reaching influence on natural ecosystems and human societies[3], which call for urgent political and economic actions to reduce greenhouse gas emissions and keep atmospheric $CO_2$ concentration below a safe level to mitigate the risk[4]. Several components of the Earth system have been identified as tipping elements that may reach or pass a tipping point when global warming exceeds a critical threshold such as

1.5 °C above preindustrial temperature[1,3]. The Earth system is a complex dynamical system with different components highly interconnected and interdependent, thus tipping in one element can lead to cascading changes in another[5–7], and even could trigger a planetary-scale tipping point[8,9].

The global hydrological cycle, particularly the global monsoon system, has been suggested to be vulnerable to climate tipping points and may experience abrupt shifts in the future[10]. However, the direction and amplitude of abrupt shifts are unclear, mainly because the available observational records are too short to provide useful information[11], and rainfall response is usually more difficult to constrain than temperature[12]. Paleoclimate records can provide the only long-term context for evaluating the impact of climate tipping points[11].

[1]School of Geography and Ocean Science, Nanjing University, Nanjing, China. [2]Department of Physical Geography and Ecosystem Science, Lund University, Lund, Sweden. [3]Department of Physical Geography and Bolin Centre for Climate Research, Stockholm University, Stockholm, Sweden. [4]Regional Climate Group, Department of Earth Sciences, University of Gothenburg, Gothenburg, Sweden. [5]Department of Earth and Atmospheric Sciences, University of Quebec in Montreal, Montreal, QC, Canada. [6]Earth System Modelling, School of Engineering and Design, Technical University of Munich, Munich, Germany. [7]Potsdam Institute for Climate Impact Research, Potsdam, Germany. [8]National Oceanography Centre, Southampton, UK. ✉e-mail: huayulu@nju.edu.cn
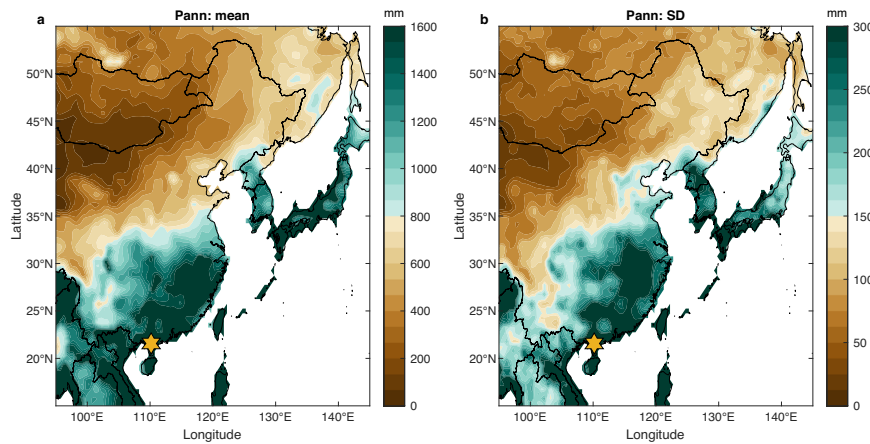
**Fig. 1 | Spatial pattern of annual rainfall and its variability in East Asia. a** Spatial distribution of the mean of annual rainfall (Pann) in the period 1951–2020 CE. **b** Spatial distribution of the standard deviation (SD) of annual rainfall in the same period. The hexagons indicate the location of Qingtongyang Maar Lake in this study. The gridded monthly rainfall data version 2022 from the Global Precipitation Climatology Centre (GPCC) with a spatial resolution of 0.5° × 0.5°[44] were used for analysis.

However, the precision, resolution, and spatial coverage of paleoclimate records are insufficient and need to be improved[11]. In the EASM domain, our understanding of paleomonsoon evolution mainly depends on the precisely-dated speleothem $\delta^{18}O$ records[13]. However, the interpretation of speleothem $\delta^{18}O$ records in East Asia remains debated, excluding it as a local rainfall proxy[13–16]. For instance, a speleothem trace-element record from Haozhu Cave in central-eastern China suggested wetter conditions during North Atlantic cold stadials when speleothem $\delta^{18}O$ records indicated a weaker summer monsoon[15]. The situation is further complicated by inconsistent results of other proxy records in the same region[17–21]. Besides, the nonlinear behavior of the EASM is understudied, making it unclear whether changes in the EASM rainfall are gradual or abrupt. The potential for abrupt shifts in the EASM rainfall under excessive global warming were largely overlooked in both assessment reports and academic literature[1,3,22,23]. Absent from these debates is an independent quantitative reconstruction of past rainfall changes in the EASM realm, particularly in southern China. Southern China is the core region of EASM influence where annual rainfall exceeds 800 mm and rainfall variability is the largest (Fig. 1).

In this study, we aim to provide a robust reconstruction of the EASM rainfall in southern China and use it to detect tipping points in the EASM rainfall since the LGM and assess the cascading impacts of climate tipping points on the EASM rainfall. The first goal is achieved by applying nine statistical and machine learning methods to retrieve rainfall signals from multi-proxy records of a maar lake in southern China. Our analysis indicates that the rainfall variability at the lake location is representative of rainfall variability in southern China (Supplementary Fig. 1). The second goal is realized by comparing a large number of proxy records with multi-model simulations. We focus on two well-known tipping elements, the AMOC and Saharan vegetation cover[1,3]. The AMOC has a strong impact on global climate by conveying surface warm water northward and deep cold water southward, redistributing the solar energy received by the Earth[24]. Through its impact on the interhemispheric thermal gradient, the AMOC can alter the position and intensity of low-latitude rainfall systems, including the intertropical convergence zone (ITCZ) and the EASM[25,26]. In situ observations indicate that the AMOC has weakened during recent decades[27], and the sea surface temperature (SST) fingerprint suggests that this weakening trend extends back to the mid-20th century[28]. Climate models further project the AMOC to weaken under future anthropogenic warming[29]. Recent studies even warn that the AMOC may collapse in the coming decades[30,31]. However, the climatic impact of AMOC collapse in the context of anthropogenic warming remains unclear. The last deglaciation is characterized by a large increase in the atmospheric $CO_2$ concentration and abrupt shifts in the AMOC[32], providing an ideal analog for examining its future influence. The Sahara is currently the largest hot desert and source of dust emission on Earth, which plays a crucial role in regulating global climate and biophysical feedbacks[33]. Paleoenvironmental records indicate the greening of the Sahara during the African Humid Period (AHP) when the African summer monsoon intensified and rainfall increased in response to higher summer insolation[34]. Conversely, the termination of the AHP and collapse of Saharan vegetation during the mid- to late Holocene are an abrupt event occurring faster than orbital forcing[10,34,35], which is a paradigm for going through climate tipping points[1]. Recent studies suggest that the changes in Saharan vegetation cover and dust emissions can not only influence local climate in northern Africa[36] but also the distant climates ranging from the tropics[37,38] to the Arctic[39]. The Asian summer monsoon could be affected by Saharan vegetation changes through large-scale atmospheric circulation such as the upper-level Rossby wave train and the Pacific Walker circulation[40,41]. However, the timing, amplitude, and structure of EASM rainfall changes in response to the end of the Green Sahara and AHP are not well defined due to the lack of high-resolution quantitative rainfall records. Given that the Sahara/Sahel vegetation and the West African monsoon have been identified as a tipping element that may experience abrupt shifts under future anthropogenic warming[1,3], investigating the effect of Saharan vegetation change during the past will have practical implications for better understanding of vegetation feedback on future climate.

## Results and discussion
### Ensemble reconstruction of the EASM rainfall
Quantitative paleoclimate reconstructions are closely related to climate proxy and reconstruction methodology[42,43]. We, therefore, employ a multi-proxy, multi-method probabilistic framework to generate a large ensemble for robust reconstruction of the EASM rainfall. The reconstruction target is anomalies in the annual rainfall (Pann) relative to 1961–1990 CE. The period 1953–2005 CE was chosen for calibration because it has the most complete climate data and overlaps with the proxy data. The period before 1953 CE was not used for calibration due to significant uncertainty in the climate data. However, gridded rainfall data from the Global Precipitation Climatology Centre (GPCC)[44] was utilized as an additional independent validation of our reconstructions. Because annual rainfall in East Asia is dominated by summer monsoon rainfall and their changes are highly correlated with similar amplitudes (Supplementary Fig. 2), we only reconstruct the

annual rainfall. To preserve the full amplitude of rainfall variability and avoid spurious signals, both rainfall observations and proxy records were decadally smoothed with a cubic-smoothing spline[45] to have roughly the same frequency (Supplementary Fig. 3), following the suggestion of previous studies[46–48]. Smoothing can also enhance the signal-to-noise ratio and stabilize the relationship between climate and proxies, reducing the impact of age model uncertainty (Supplementary Fig. 4). From a sedimentological perspective, smoothing is necessary because climate signal is naturally smoothed during the deposition of lake sediments, and lake records are unable to capture the year-to-year climate variability as precisely as tree-ring records[47,48].

In November 2016, a sediment core (QTY-2-1) was recovered from the center of the Qingtongyang Maar Lake (110°10′E, 20°34′N, 131 m above sea level) in the Leizhou Peninsula, southern China. This lake is a closed-basin crater lake with a very small catchment and lack of river input, making it a natural gauge for past rainfall amount change. The core was split and subject to high-resolution color extraction and X-ray fluorescence (XRF) element scanning (Methods). The age model of the core is based on linear interpolation and extrapolation of the median values of sixteen AMS (accelerator mass spectrometry) $^{14}$C dates with two outliers excluded, which have been calibrated to calendar years before present (BP), where present refers to 1950 CE (Methods, Supplementary Table 1, and Supplementary Fig. 5). The age model over the past 150 years is constructed by the piecewise constant rate of supply (CRS) model[49] of $^{210}$Pb dates constrained by the $^{137}$Cs peak at 1963 CE and two post-bomb $^{14}$C dates at 1955 CE and 2014 CE (Supplementary Fig. 6). The full ranges of these post-bomb $^{14}$C dates are only 2 to 3 years (Supplementary Table 1), ensuring a precise age model and allowing for meaningful calibration with rainfall observations on the decadal time-scale. Even when assuming a larger age uncertainty by treating the full age range as one standard error and applying Bayesian age modeling to assess its impact, the rainfall-proxy relationship remains robust, regardless of changes to the age model (Supplementary Fig. 4).

Four climate-proxy records with nearly annual to decadal time-resolution were used as predictors for quantitative rainfall reconstructions, including the color b* and the concentrations of iron (Fe), manganese (Mn), and calcium (Ca) (Fig. 2). Color b* is a proxy for the concentration of goethite and hematite in lake sediment[50]. Fe and Mn concentrations are sensitive proxies for redox conditions in the lake at the time of sediment deposition[51]. Ca concentration indicates the content of carbonate in lake sediment[52]. Therefore, they are excellent indicators of past rainfall changes (Supplementary Discussion). Both correlation and partial-correlation analyses indicate a significant correlation with rainfall ($P < 0.02$) but a poor correlation with temperature during the calibration period 1953–2005 CE when accounting for the degrees of freedom (Supplementary Table 2), demonstrating that rainfall is the dominant controlling factor of changes in these proxy records and thus can be faithfully reconstructed. We used the expressed population signal (EPS)[53] and mean inter-series correlation (Rbar)[53] to evaluate the common variance of these proxy records over time with a sliding window of 3000 years. The EPS is a measure of how well a finite number of proxy records represents an infinite population chronology[53]. The Rbar indicates the average correlation between all possible pairs of proxy records[53]. The persistent positive values of sliding EPS and Rbar quantitatively indicate that these proxy records respond to a common climate signal and the proxy-climate relationships remain stable over time (Fig. 2e). Our results indicate that the four proxy records from the Qingtongyang Maar Lake exhibit synchronous changes over the past 22,000 years, especially during the last deglaciation and mid-to-late Holocene when abrupt climate changes occurred, which is supported by higher EPS and Rbar values (Fig. 2). All proxy records show low values during the Bølling–Allerød (BA) interstadial and the early to middle Holocene, which qualitatively indicates anaerobic conditions in the lake and increased freshwater input (Supplementary Discussion).

Our rainfall reconstruction ensemble consists of 14,850 members that account for uncertainties in the reconstruction method, proxy measurement, proxy selection, calibration period, weighting scheme, and regression residual. We use nine statistical and machine learning methods to reconstruct rainfall: composite plus scaling (CPS) and principal component regression (PCR) and their variants, i.e., optimal information extraction (OIE) and point-by-point regression (PPR), partial least squares (PLS) regression and two regularization methods, i.e., ridge regression (RIG) and elastic net (ELN), as well as two machine learning methods, i.e., artificial neural network (ANN) and convolutional neural network (CNN) (Methods). All methods use the same proxy matrix as input and each generates 1650 members of reconstruction. Cross-validations indicate that these methods have excellent performance in reconstructing rainfall variability, with the regularization and machine learning methods showing superior performance and a narrower range of uncertainties (Supplementary Table 3 and Supplementary Fig. 7). The rainfalls reconstructed by these methods closely track station-based rainfall observations during the period 1953–2005 CE and the GPCC rainfall during the period 1891–2005 CE (Supplementary Fig. 8).

## Abrupt shifts in the EASM rainfall since the LGM

The rainfall reconstructions obtained by the nine methods exhibit similar oscillations on the decadal to millennial timescales over the past 22,000 years (Fig. 3 and Supplementary Figs. 8, 9), indicating that our reconstruction is robust to the methodology used. Based on the framework of ensemble reconstruction, we consider as many uncertainties as possible when quantitatively reconstructing the EASM rainfall (Methods). The influence of age model uncertainty has also been considered. The age model uncertainty mainly affects the weights of proxy records and the timings of abrupt climate changes (Supplementary Fig. 4). Therefore, we addressed this uncertainty by randomly adjusting proxy weights during reconstruction and applying Bayesian age modeling to ascertain the timings of abrupt shifts (Methods). Even after accounting for these uncertainties, the amplitudes of rainfall changes in our reconstructions during the past 22,000 years are still larger than the total uncertainties (Fig. 3 and Supplementary Figs. 8, 9), demonstrating that the reconstructed rainfall changes are significantly better than the stochastic process.

Consistent with the physical and chemical interpretations of the proxy records (Fig. 2 and Supplementary Discussion), all the quantitative reconstructions indicate that the EASM rainfall was most abundant during the BA interstadial and the early-middle Holocene, with rainfall amounts being ~440 mm (28%) higher than the modern value of 1592 mm in the period 1961–1990 CE. The rainfall was substantially lower during the LGM, Heinrich Stadial 1 (HS1), Younger Dryas (YD), and late Holocene, with the lowest rainfall occurring during the HS1. The general trend of the EASM rainfall evolution revealed by our reconstructions is consistent with the pattern of summer insolation change in the Northern Hemisphere, which peaked during the early Holocene (Fig. 3). However, unlike the gradual change in summer insolation, our rainfall reconstructions strongly suggest that the EASM rainfall was characterized by contrasting stable states and abrupt transitions between these states. Based on the regime shift analysis[54,55] (Supplementary Fig. 10), the evolution of the EASM rainfall over the past 22,000 years can be divided into six major climate states (or periods) that have different characteristics and internal dynamics, aligning with the LGM, HS1, BA, YD, early-middle Holocene, and late Holocene. The rainfall anomalies relative to the mean of 1592 mm in the period 1961–1990 CE during these periods are 141 ± 97 mm, −1 ± 98 mm, 447 ± 86 mm, 53 ± 89 mm, 440 ± 75 mm, and 102 ± 105 mm, respectively. Between two adjacent climate states are abrupt and irreversible shifts in rainfall amounts. Here, "abrupt" indicates that the change in a system is substantially faster than the rate of its past change, while "irreversible" indicates that the system does not
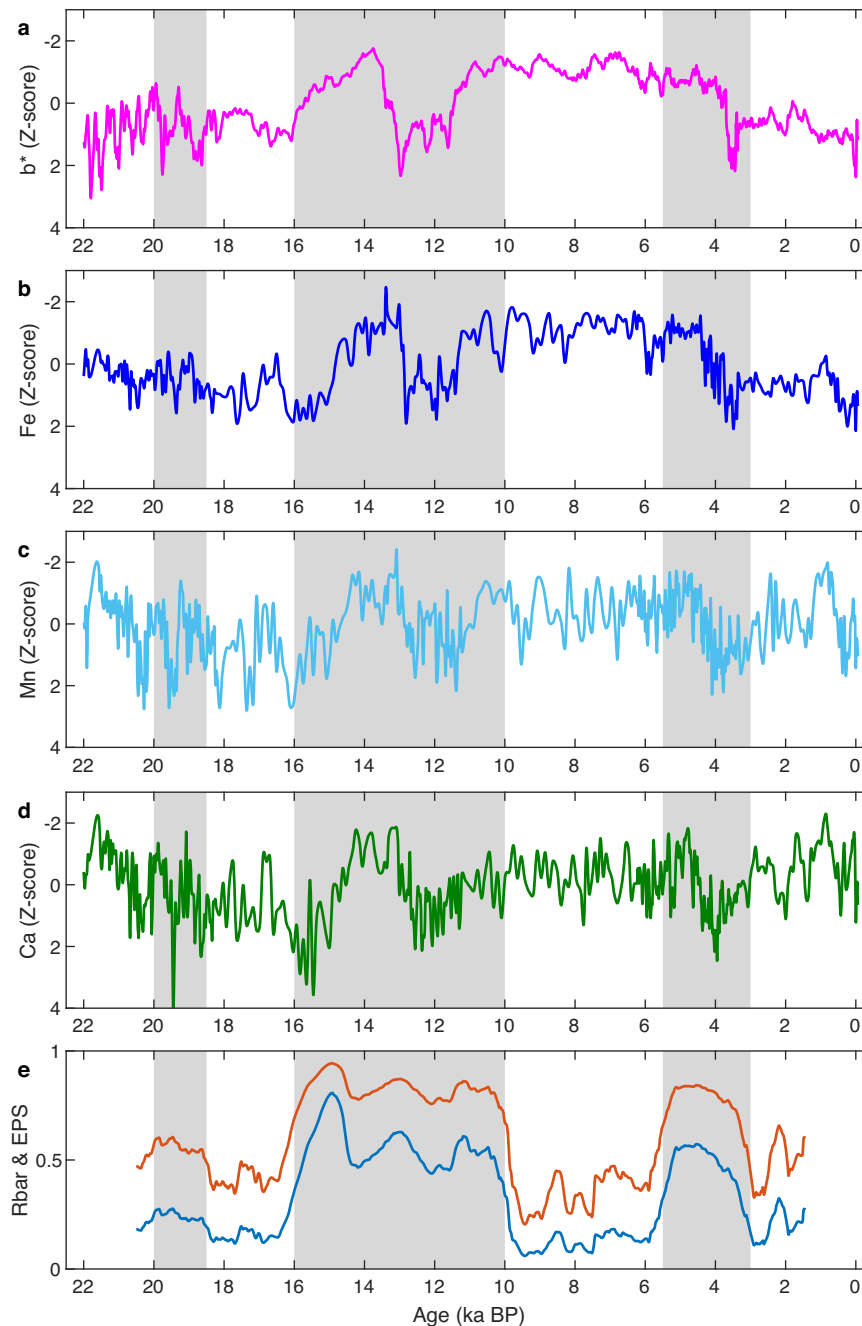
**Fig. 2 | Multi-proxy records from the Qingtongyang Maar Lake over the past 22,000 years. a** Color b*. **b** Fe concentration. **c** Mn concentration. **d** Ca concentration. **e** The running mean correlation coefficient between all pairs of proxy records (Rbar, blue) and the expressed population signal (EPS, orange). The gray shadings indicate time intervals with high Rbar and EPS values and, thus, a strong common signal in the proxy records. All proxy records have been normalized to have zero mean and standard deviation units (Z-score) over the entire period for better comparison. Source data are provided as a Source Data file.

recover to its previous state immediately after shift, but remains in a new state for a long time (>1000 years in this study) until its next shift[10]. Based on the Bayesian age modeling of our $^{14}$C dates from the Qingtongyang Maar Lake (Methods), the timings of these abrupt shifts are estimated to be centered at 18860 ± 310, 14640 ± 400, 12870 ± 290, 11360 ± 170, and 4370 ± 60 yr BP (Supplementary Table 4). The transition from the HS1 to the BA is characterized by an abrupt increase in rainfall by 448 mm, while the transitions into and out of the YD are characterized by abrupt changes in rainfall by 394 mm and 387 mm, respectively. The transition from middle to late Holocene is characterized by a decrease in rainfall by 338 mm. The amplitude of rainfall decrease from the LGM to the HS1 is relatively small, with an amplitude

of 142 mm, possibly because the rainfall amount during the LGM was low. Nonetheless, all rainfall changes are statistically significant at the 95% confidence level based on the two-tailed two-sample $t$-test (Supplementary Fig. 10). These abrupt shifts can be identified by another objective method, the Bayesian change-point analysis[56], which further supports our finding based on the regime shift analysis (Supplementary Fig. 10). These two independent methods are consistent in revealing the timings and structures of abrupt shifts in the EASM rainfall in most cases, but the Bayesian method can provide more details about the abrupt shift during the mid-to-late Holocene transition. Based on the Bayesian change-point analysis, the mid-to-late Holocene transition is characterized by an abrupt drop of rainfall with
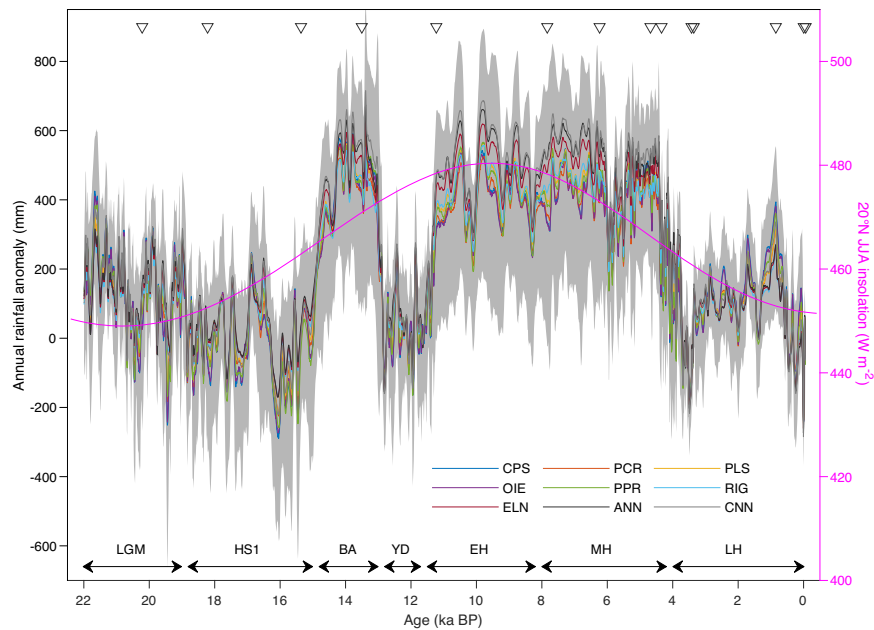
**Fig. 3 | Ensemble reconstruction of the East Asian summer monsoon (EASM) rainfall over the past 22,000 years.** The annual rainfall anomaly is expressed as deviations from the mean value of 1592 mm in the period 1961–1990 CE. The gray shading indicates the 95% confidence interval (from 2.5th to 97.5th percentile) of the reconstructions based on all methods ($N = 14{,}850$). The lines with different colors indicate the means of the reconstruction based on different methods

($N = 1650$). The triangles on the top indicate radiocarbon ($^{14}$C) age-control points. The daily mean of solar insolation at 20°N during summer (June-July-August, JJA)[64] is shown for comparison. LGM, Last Glacial Maximum; HS1 Heinrich stadial 1, BA Bølling–Allerød, YD Younger Dryas, EH early Holocene, MH mid-Holocene, LH late Holocene. Source data are provided as a Source Data file.

an amplitude of -140 mm at $4370 \pm 60$ yr BP and a subsequent less abrupt but persistent decrease in rainfall with an amplitude of 416 mm until $3290 \pm 70$ yr BP (Supplementary Fig. 10 and Supplementary Table 4). Therefore, our reconstruction reveals a two-step abrupt shift in the EASM rainfall during the mid-to-late Holocene transition, which has implications for a better understanding of the forcing mechanisms and cultural consequence of the well-known 4.2 ka event[41,57].

To test the representativeness of our rainfall reconstruction, we compare our reconstruction with other proxy records from the same region, including the Huguangyan and Tianyang maar lakes (Supplementary Fig. 11). Although the proxy records from Huguangyan and Tianyang have much lower temporal resolution, millennial-scale events such as the HS1 and YD are clearly identified, supporting that the abrupt shifts in our rainfall reconstruction are regional phenomena rather than local noises. We also make a comprehensive compilation of paleoclimate records from the whole EASM domain (Methods), which consistently indicate that abrupt shifts in the rainfall regime are a continental-scale feature and intrinsic mode of the EASM rainfall variability since the LGM (Supplementary Tables 5–9 and Supplementary Figs. 12, 13). To help better understand the climatic significance of speleothem $\delta^{18}O$ records in East Asia, we compare our rainfall reconstruction with the speleothem $\delta^{18}O$ records from Dongge and Hulu caves in southern China (Supplementary Fig. 11d). The strong similarity between them during the last deglaciation indicates that the speleothem $\delta^{18}O$ records in East Asia might be indeed related to hydroclimate changes during this period. After accounting for the effect of global ice volume change, the speleothem $\delta^{18}O$ values during the LGM are slightly lighter than those during the late Holocene. This is consistent with our reconstruction indicating higher rainfall amounts during the LGM than in the late Holocene. However, the changes in speleothem $\delta^{18}O$ records during the Holocene are much more gradual, indicating decoupled changes between speleothem $\delta^{18}O$ records and the East Asian hydroclimate. Previously, the speleothem $\delta^{18}O$ records in East Asia were interpreted as monsoon wind intensity, which is positively (negatively) correlated with monsoon rainfall in northern

(southern) China[58]. However, the decoupled changes between speleothem $\delta^{18}O$ records and our rainfall reconstruction, as well as other hydroclimate records in East Asia, indicate that speleothem $\delta^{18}O$ records are not a direct signal of monsoon rainfall.

## AMOC forcing of EASM rainfall during the last deglaciation

The EASM rainfall change can be driven by both dynamic and thermodynamic components[59], with the former related to monsoon circulation and the latter related to atmospheric water vapor. The global mean temperature during the LGM was 6.1 °C (95% confidence interval: 5.7–6.5 °C) cooler than that during the late Holocene[60], and the associated thermodynamic effect was expected to reduce atmospheric water vapor content and thus lead to less rainfall in East Asia. However, our reconstruction indicates that the rainfall amount in southern China during the LGM was similar to or even higher than that during the late Holocene (Fig. 3). This finding suggests that the global mean temperature change may not be the dominant control of the EASM rainfall anomaly during the LGM, at least in the core monsoon region. Moreover, the reconstructed rainfall changes during the last deglaciation did not follow the gradual increasing trend in the global mean temperature[61,62] and atmospheric $CO_2$ concentration[63] (Fig. 4). Therefore, the observed variability in EASM rainfall is likely caused by other mechanisms, rather than a simple response to the thermodynamic effect of changes in the global mean temperature.

The only climatic forcing that shared similarity between the LGM and late Holocene is the local summer insolation at 20°N[64] (Fig. 3). We, therefore, attribute the similar rainfall amounts to the dynamic effect of nearly identical summer insolation, which could compensate for the thermodynamic effect of global mean temperature through changes in the land-sea thermal contrast and latitudinal temperature gradient. However, insolation forcing alone cannot explain the EASM rainfall changes during the last deglaciation when the EASM rainfall was punctuated by two millennial-scale drought events (i.e., HS1 and YD) at times of high summer insolation (Fig. 3). In contrast, the oscillation of deglacial EASM rainfall was in parallel with the AMOC strength[65] and
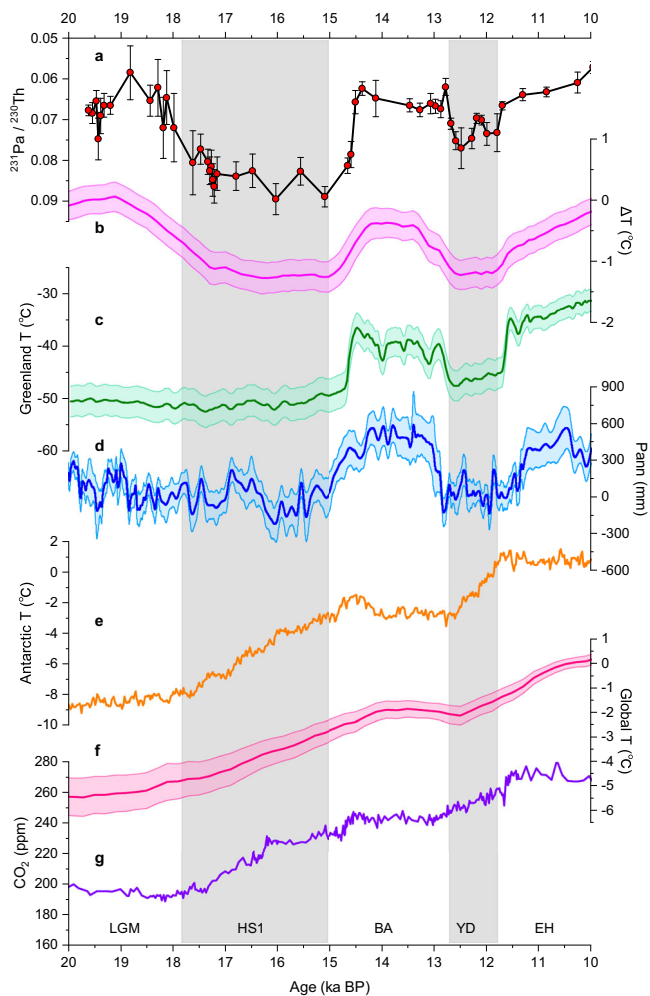
**Fig. 4 | Comparison of East Asian summer monsoon (EASM) rainfall to the Atlantic meridional overturning circulation (AMOC) and the global temperature during the last deglaciation. a** Sediment ²³¹Pa/²³⁰Th ratio with 1σ uncertainty from Bermuda rise in the deep western subtropical Atlantic, a kinematic proxy for the AMOC[65]. **b** Proxy-based reconstruction of the temperature difference between the Northern Hemisphere and the Southern Hemisphere with 1σ uncertainty[61]. **c** Stacked temperature reconstruction with 1σ uncertainty based on three ice cores from Greenland[67]. **d** Ensemble rainfall reconstruction with 1σ uncertainty from Qingtongyang Maar Lake (this study). **e** Stacked temperature reconstruction based on five ice cores from Antarctic[68]. **f** Proxy-based reconstruction of the global mean temperature with 1σ uncertainty[62]. **g** Atmospheric $CO_2$ concentration record from an ice core in the West Antarctic Ice Sheet Divide[63]. LGM Last Glacial Maximum, HS1 Heinrich Stadial 1, BA Bølling–Allerød, YD Younger Dryas, EH early Holocene.

the interhemispheric temperature gradient[61] (Fig. 4), indicating a dominant role of the AMOC forcing. The AMOC has experienced tipping points for abrupt transition between strong states and weak states during the last deglaciation[65], which could have strong impacts on the EASM rainfall[15,66]. For instance, remarkable weakening of the AMOC during the HS1 and YD[65] reduced northward heat transport and generated a bipolar temperature seesaw pattern, with cooling in the Greenland[67] and Northern Hemisphere and warming in the Antarctic[68] and Southern Hemisphere, which diminished the interhemispheric temperature gradient[61] and forced the ITCZ to move southward, reducing rainfall in East Asia (Fig. 4). Comparison of our rainfall reconstruction with hydroclimate records along a north-south transect across the East Asian-Australian monsoon system reveals an opposite rainfall pattern between the two hemispheres during the last deglaciation (Supplementary Fig. 14), supporting a southward migration of the ITCZ mean position during the HS1 and YD in response to the

weakening of the AMOC during the HS1 and YD[26,69]. The cooling of the North Atlantic during the HS1 and YD can also influence the EASM rainfall via changes in the intensity and position of the westerlies[15,66,70].

However, the spatial pattern of EASM rainfall response to abrupt shifts in the AMOC during the last deglaciation remains ambiguous due to the lack of a systematic analysis of both proxy records and climate simulations. For instance, a recent study based on a trace-element record from Haozhu Cave and a hosing experiment under preindustrial conditions suggests that central-eastern China was wet (dry) during the times of a weak (strong) AMOC and the rainfall anomaly in East Asia exhibited a tripole mode[15]. The Haozhu record further indicates that the climate during the LGM was wetter than that of the early Holocene[15]. However, a wetter central-eastern China during North Atlantic cold events and LGM is challenged by other proxy records from the same region[17–21], including two trace-element records from Heshang Cave[17] and Hulu Cave[21]. Moreover, another hosing experiment under the LGM boundary conditions indicates rainfall decrease rather than increase in central-eastern China in response to the weakening of the AMOC[66], which highlights the need for multi-model comparison. Previous studies mainly focused on the response of EASM rainfall to the weakening of the AMOC but overlooked the impact of AMOC strengthening. However, the responses of climate to the weakening and strengthening of the AMOC may not be a reversed process. In particular, abrupt shifts in the AMOC during the last deglaciation were accompanied by variations in other climatic forcings such as solar insolation, ice sheet, and greenhouse gas concentrations. Therefore, it is necessary to analyze the individual characteristics of EASM rainfall response during both the transitions into and out of HS1 and YD, which has not yet been done. Here we collect a large number of hydroclimate records in East Asia based on rigorous criteria (Methods, Supplementary Tables 5–8) and compare them with a state-of-the-science isotope-enabled transient climate experiment (iTRACE)[16] and an earlier version without isotope module (TRACE-21ka)[71] (Methods). Although continuous records with good age control and high temporal resolution are scarce for the last deglaciation, the general trend of hydroclimate change can be roughly inferred from these proxy fragments.

From LGM to HS1, the majority of proxy records, including the trace-element record from Haozhu Cave[15], indicate a drying climate over East Asia, except for two proxy records from southeastern China[72,73], which indicate a wetting climate (Fig. 5a–c and Supplementary Table 5). In contrast to the proxy records, the iTRACE simulation indicates that both annual and summer rainfalls increased during the HS1 relative to the LGM over Mongolia and eastern China (Fig. 5a, b). In the TRACE-21ka simulation, the annual and summer rainfalls increased in northern China and northeastern China but decreased in southern China (Supplementary Fig. 15a, b). Since it has been suggested that autumn rainfall could contribute to the changes in East Asian hydroclimate[74], we also analyze the response to autumn rainfall. Indeed, the magnitude of autumn rainfall variability is comparable to that of summer rainfall and even larger (Fig. 5c). The decrease in autumn rainfall in northeastern China can partly explain the discrepancy between proxy records and model simulations in this region, but not for that in northern China and southern China. As revealed by sensitivity experiments, the summer rainfall variability in northern China is driven primarily by summer insolation and secondarily by meltwater, while summer rainfall variability in southern China is driven primarily by meltwater and secondarily by summer insolation[16]. In the iTRACE simulation, the increasing summer insolation during the HS1 tends to increase summer rainfall in northern China and northeastern China but decrease summer rainfall in southern China, while the weakened AMOC tends to decrease summer rainfall in northern China and northeastern China but increase summer rainfall in southern China[16]. As a consequence, summer rainfall in the whole of eastern China increased during the HS1 in the iTRACE
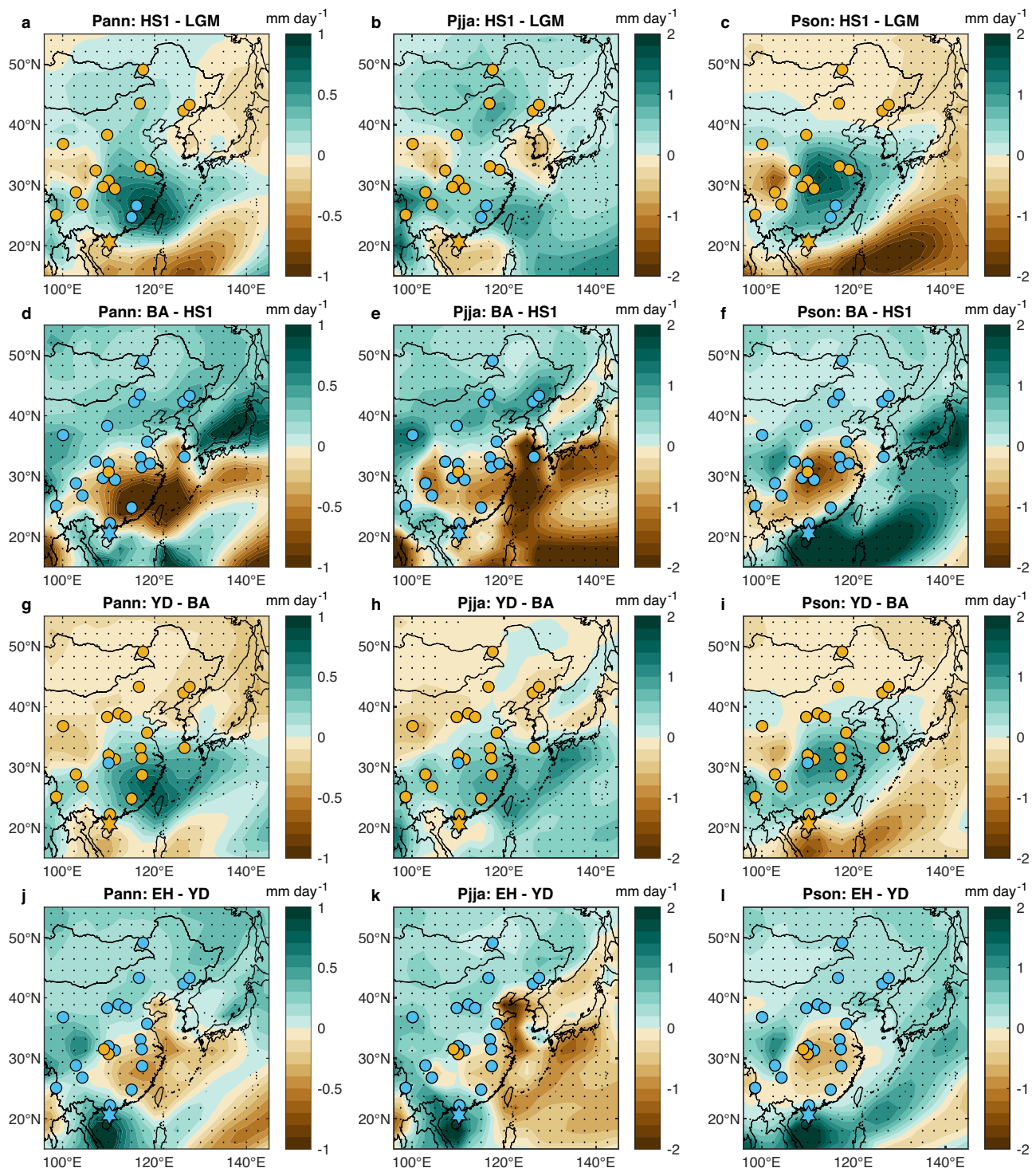
**Fig. 5 | Response of rainfall in East Asia to the weakening and strengthening of the Atlantic meridional overturning circulation (AMOC) during the last deglaciation in an isotope-enabled transient climate experiment (iTRACE)[16].** The maps show rainfall differences between HS1 and LGM (**a–c**), BA and HS1 (**d–f**), YD and BA (**g–i**), EH and YD (**j–l**). Pann: annual rainfall; Pjja: summer rainfall; Pson: autumn rainfall. Brown (blue) hexagrams (this study) and circles indicate proxy records with drying (wetting) climate during these events. Stippling indicates the areas where rainfall changes are significant at 95% confidence level based on the two-tailed two-sample *t*-test. LGM Last Glacial Maximum, HS1 Heinrich Stadial 1, BA Bølling–Allerød, YD Younger Dryas, EH early Holocene.

simulation (Fig. 5b). However, such a response of EASM rainfall in the iTRACE simulation may not be realistic as it is inconsistent with the currently available proxy records (Supplementary Table 5) and there are large uncertainties in simulating rainfall response in East Asia to meltwater forcing[75]. We argue that the effect of AMOC slowdown on the global summer climate during HS1 might have been

underestimated. For instance, summer cooling during the HS1 is limited to the North Atlantic in the iTRACE simulation, and the Eurasian continent experiences summer warming (Fig. 6b). The warming of the Eurasian continent may have been responsible for the simulated rainfall increase in East Asia during the HS1. However, a recent reconstruction of summer temperature in northeastern China based
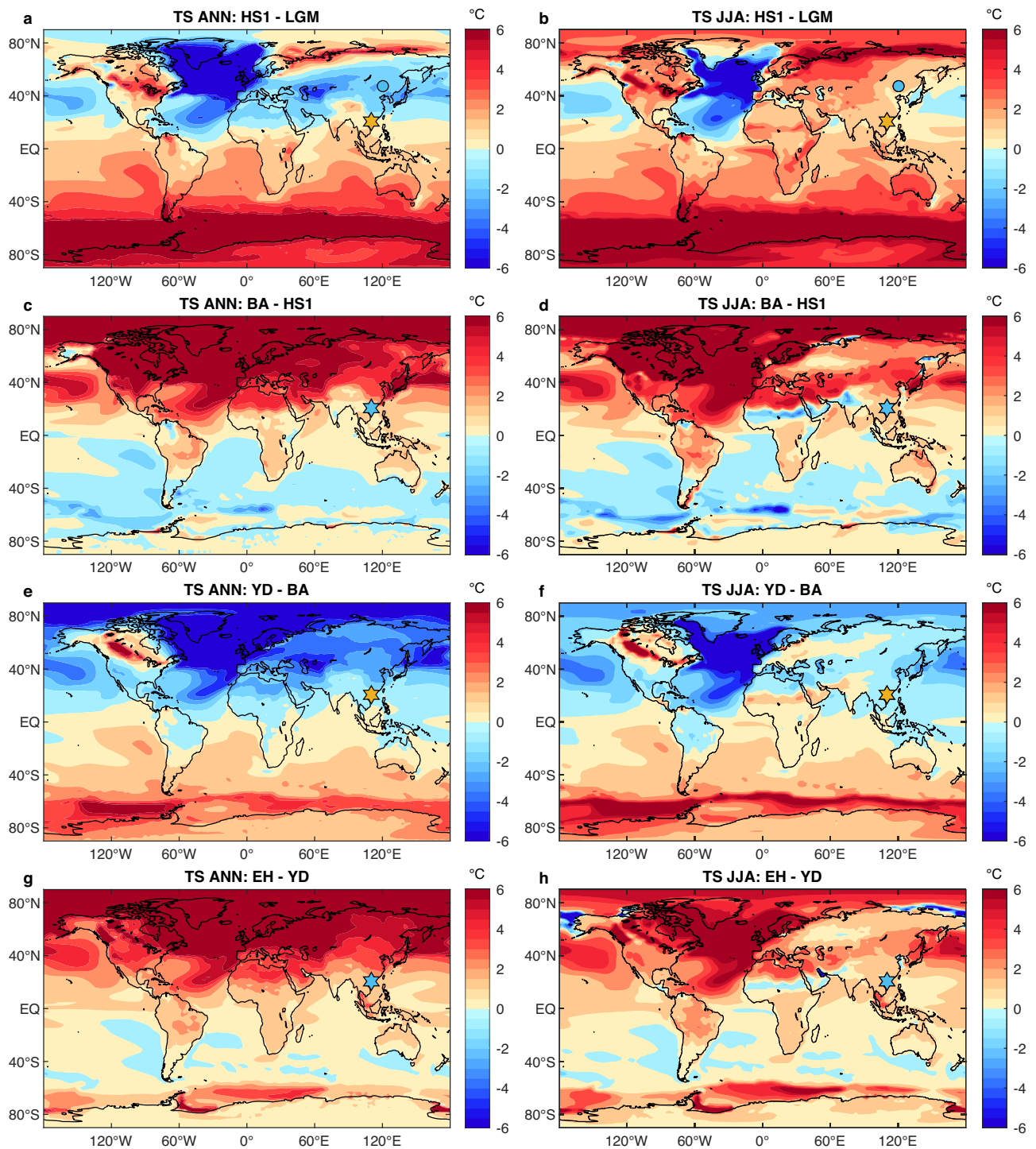
**Fig. 6 | Response of global temperature to the weakening and strengthening of the Atlantic meridional overturning circulation (AMOC) during the last deglaciation in an isotope-enabled transient climate experiment (iTRACE)[16].** The maps show annual (ANN) and summer (JJA) surface temperature (TS) differences between HS1 and LGM (**a**, **b**), BA and HS1 (**c**, **d**), YD and BA (**e**, **f**), EH and YD (**g**, **h**). Brown (blue) hexagrams indicate the Qingtongyang Maar Lake with a drying (wetting) climate during these events. Blue circles indicate the Arxan Lake with summer cooling during the HS1[76]. LGM Last Glacial Maximum, HS1 Heinrich Stadial 1, BA Bølling–Allerød, YD Younger Dryas, EH early Holocene.

on the distribution of branched glycerol dialkyl glycerol tetraethers (brGDGTs) in the sediment core from the Arxan Lake indicates substantial summer cooling during the HS1[76].

From HS1 to BA, all proxy records, except for the trace-element record from Haozhu Cave[15], indicate a wetting climate over the whole of East Asia (Fig. 5d–f and Supplementary Table 6). The iTRACE simulation shows that both annual and summer rainfalls, as well as

autumn rainfall, increased in northeastern China and northern China but decreased in southern China during the BA period (Fig. 5d–f). Similar to the iTRACE simulation, annual and autumn rainfalls in southern China decreased during the BA in the TRACE-21ka simulation, but summer rainfall increased in both northern and southern China (Supplementary Fig. 15d–f). The global temperature during the transition from HS1 to BA is characterized by strong warming in the
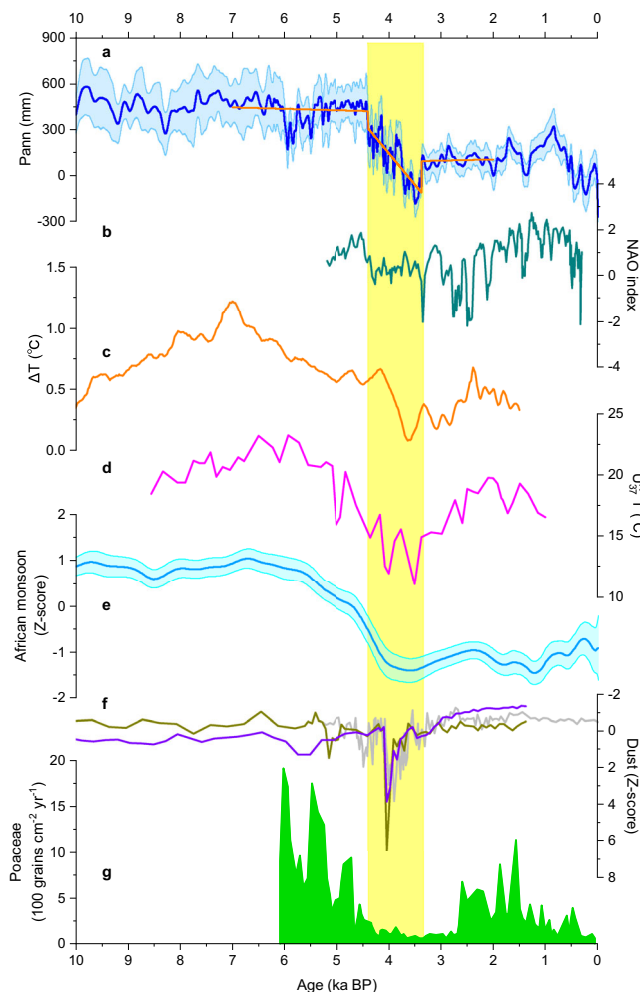
**Fig. 7 | Link rainfall change to the end of the Green Sahara and related climate feedbacks during the mid- to late Holocene. a** Ensemble rainfall reconstruction with 1σ uncertainty from Qingtongyang Maar Lake (this study). The orange line indicates piecewise linear trends based on Bayesian change-point analysis[56]. **b** Reconstruction of North Atlantic Oscillation (NAO) index based on lake record from southwestern Greenland[92]. **c** Temperature difference between extratropical Northern Hemisphere (30°N–90°N) and Southern Hemisphere (30°S–90°S)[90]. **d** Alkenone-based summer temperature reconstruction from Qinghai Lake in northeastern Tibetan Plateau[96]. **e** Integrated African summer monsoon index with 1σ uncertainty based on six leaf wax hydrogen isotopic composition ($\delta D_{wax}$) records (Methods, Supplementary Table 10). **f** Normalized dust records based on dolomite (brown) and carbonate (purple) from the Gulf of Oman[86] and Ca/Ti ratio (gray) from the Nile Delta[85]. **g** Saharan vegetation cover change as reflected by the influx rate of Poaceae pollen from Lake Yoa[83].

Northern Hemisphere with small cooling in the Southern Hemisphere and weak warming in Antarctica (Fig. 6c, d), while the transition from LGM to HS1 is characterized by strong cooling in the North Atlantic and strong warming in the Southern Hemisphere (Fig. 6a, b). These evidences suggest that the climatic transition from HS1 to BA is not a simple reverse of the transition from LGM to HS1.

From BA to YD, all proxy records, except for the trace-element record from Haozhu Cave[15], indicate a drying climate over the whole of East Asia (Fig. 5g–i and Supplementary Table 7). The iTRACE simulation shows that annual, summer, and autumn rainfalls significantly increase in southern China, southwestern China, and North China Plain, but decrease in northeastern China, semi-arid northern China, and north-eastern Tibetan Plateau (Fig. 5g–i). The simulated summer rainfall in the northern part of northeastern China also increased during the YD, but not significantly. The TRACE-21ka simulation shows rainfall

increase in both northern and southern China (Supplementary Fig. 15g–i). The global temperature during the transition from BA to YD is characterized by strong cooling in the Northern Hemisphere and strong warming in the Southern Hemisphere (Fig. 6e, f). Unlike the temperature response during the HS1, the simulated summer cooling during the YD is not limited to North Atlantic, and the summer temperature in East Asia decreased during the YD in the iTRACE simulation (Fig. 6f). This difference may explain the better agreement between proxy records and model simulation during the YD than HS1.

From YD to early Holocene, all proxy records, except for a trace-element record from Haozhu Cave[15] and a hopanoid record from Dajiuhu peatland[77], indicate a wetting climate over the whole of East Asia (Fig. 5j–l and Supplementary Table 8). This pattern is generally consistent with the model results from the TRACE-21ka simulation (Supplementary Fig. 15j–l). The rainfall response at that time in the iTRACE simulation is in good agreement with proxy records from northeastern China, northern China, southwestern China, and the Leizhou Peninsula (Fig. 5j–l). However, the iTRACE simulation shows a rainfall decrease in southeastern China where various proxy records indicate an increasing rainfall. This divergence is robust and cannot be attributed to shortcomings in proxy records, because a well-dated speleothem carbon isotope ($\delta^{13}C$) record from Shennong Cave clearly indicates higher rainfall during the early Holocene than the YD[78]. The transition from YD to early Holocene in the iTRACE is characterized by warming in both the Northern and Southern Hemispheres, with the strongest warming occurring in the Northern Hemisphere (Fig. 6g, h). This pattern is generally consistent with global temperature reconstruction[61].

Taken together, there are large discrepancies between proxy records and climate model simulations in reconstructing the hydro-climate of southern China during the last deglaciation, particularly for the iTRACE simulation running with the Community Earth System Model (CESM). We argue that these discrepancies may be attributable to the inability of climate models in correctly simulating the EASM rainfall pattern. It has been suggested that the coupled general circulation models (CGCMs) have large biases in simulating the mean state of the tropical Pacific with an excessive equatorial Pacific cold tongue when compared to observations[79]. As a result, current CGCMs are unable to accurately reproduce the spatial pattern of EASM rainfall during different seasonal stages, with the rain belt shifting northward too quickly[80]. For example, the position of the spring and pre-Mei-Yu rain belts are shifted northward compared to rainfall observations, resulting in deficient rainfall in southern China[80].

## Link to the end of Green Sahara and associated feedbacks

The climate boundary conditions during the mid- to late Holocene are largely constant[81]. Therefore, abrupt shifts in EASM rainfall under gradual insolation forcing must involve strongly nonlinear feedbacks. We attribute it to the end of the Green Sahara and associated vegetation-dust-cryosphere feedbacks (Fig. 7). However, the timing of the termination of the Green Sahara has not been well defined, with previous studies showing different results[34,35]. Therefore, our first goal is to objectively estimate this timing. Based on six high-resolution and well-dated leaf wax hydrogen isotopic composition ($\delta D_{wax}$) records from the West African and East African monsoon regions (Supplementary Table 10), we generate a synthesis of African summer monsoon that considers uncertainties in both proxy measurement and age model (Methods, Fig. 7e and Supplementary Fig. 16). Based on regime shift analysis[54,55] and Bayesian change-point analysis[56], the timing of the termination of the Green Sahara is estimated to be 4620 ± 180 yr BP, after which the African summer monsoon experienced a rapid decline with the rate of change exceeding two standard deviations during the Holocene (Supplementary Fig. 16). The timing of abrupt decline in the African summer monsoon is estimated to be centered at 4350 ± 140 yr BP (Supplementary Fig. 16), statistically coinciding with abrupt rainfall
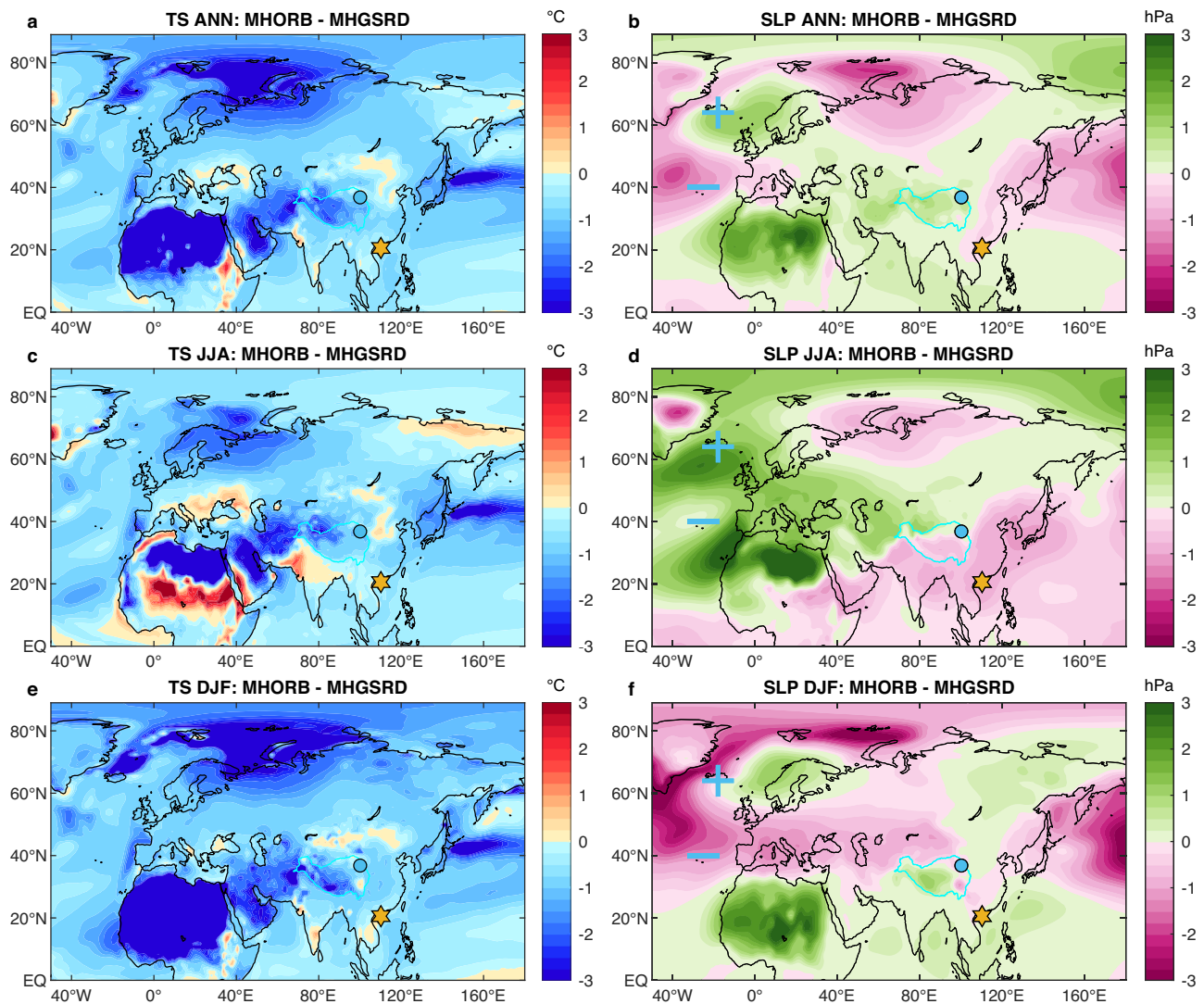
**Fig. 8 | Response of surface temperature (TS) and sea level pressure (SLP) to the end of the Green Sahara in the sensitivity experiment performed with the European Community Earth System Model (EC-Earth)[36].** The maps show annual (ANN) (**a**, **b**), summer (JJA) (**c**, **d**) and winter (DJF) (**e**, **f**) differences in the TS (**a**, **c**, **e**) and SLP (**b**, **d**, **f**) between the simulations MHORB (mid-Holocene experiment with orbital forcing only) and MHGSRD (mid-Holocene experiment with orbital forcing, a vegetated Sahara and reduced dust emissions). Brown hexagrams indicate the

Qingtongyang Maar Lake with a drying climate during the mid- to late Holocene transition (this study). Blue circles indicate the Qinghai Lake with a cooling climate during the same period. The marks "+" indicate the Icelandic Low with increasing SLP in response to the end of the Green Sahara, while the marks "−" indicate the Azores High with reducing SLP at the same time, which resembles the negative phase of the North Atlantic Oscillation (NAO−). Blue lines indicate the boundary of the Tibetan Plateau.

decrease at 4370 ± 60 yr BP in our reconstruction based on the reduced chi-square test[82] ($\chi^2 = 0.017$; $P = 0.9$). This timing also coincides with strong reductions in the tropical trees and Sahelian grassland cover in the Saharan region as evidenced by a continuous pollen record from Lake Yoa in northern Chad[83] (Fig. 7g). Similarly, these events coincide with the onset of maximum dust flux recorded in the Kilimanjaro ice core[84] and marine sediment cores from the Nile Delta[85] and the Gulf of Oman[86] (Fig. 7f), the timing of which was estimated to be centered at 4260 ± 66 yr BP[87] ($\chi^2 = 0.78$; $P = 0.46$). These evidences suggest that the abrupt reduction in the EASM rainfall during the mid- to late Holocene is synchronous with the rapid degeneration of regional vegetation and abrupt increase in dust emissions across the Sahara in response to the termination of the Green Sahara. We further examine the climatic effect of changes in the Saharan vegetation and dust by performing two sets of mid-Holocene (MH) sensitivity experiments using the European Community Earth System Model (EC-Earth): one control experiment driven by orbital forcing only (MHORB), and an idealized experiment (MHGSRD) incorporating

orbital forcing and a vegetated Sahara with reduced dust emissions (Methods).

The deterioration of vegetation at the end of the Green Sahara could influence the climate by increasing surface albedo[88] and enhancing dust mobilization[36], which jointly reduce the absorption of solar radiation and enhance radiative cooling of the troposphere. The climatic impacts of the end of the Green Sahara are not limited to northern Africa and can affect the global climate from the tropics to the poles[89]. Our sensitivity experiments suggest that the reduced vegetation cover and increased dust emissions in the Saharan region could cause global surface cooling during both summer and winter, with the most pronounced cooling occurring in northern Africa, West Asia, the Tibetan Plateau, and the northern high latitudes (Fig. 8a, c, e). The cooling of northern Africa and West Asia is directly related to the increase in local land-surface albedo and atmospheric dust concentrations[36], while the cooling of the Tibetan Plateau and northern high latitudes is linked to the amplification of cryosphere feedbacks, such as changes in snow cover and sea ice extent[39]. The

asymmetric cooling between the Northern and Southern Hemispheres due to different land-sea configurations could alter the interhemispheric temperature gradient (Fig. 7c)[90] and shift the ITCZ southward, thereby reducing the rainfall in East Asia. Additionally, the cooling of the northern high latitudes can influence the EASM rainfall through changes in the North Atlantic Oscillation (NAO). The NAO is defined as the difference in surface sea level pressure between the subpolar Icelandic Low and the subtropical Azores High, which controls the strength and direction of the westerlies and storm tracks across the North Atlantic[91]. At $4384 \pm 23$ yr BP (weighted mean), the reconstructed NAO index shifted from primarily positive phases to a weakly positive phase with intermittent strong negative phases[92] (Fig. 7b), which closely tracks the change in the EASM rainfall ($\chi^2 = 0.047$; $P = 0.83$), indicating an inherent dynamical connection between them. The shift of NAO into more negative phases in response to the termination of the Green Sahara can also be reproduced in our climate model simulations, which indicate increasing sea level pressure in the northern Europe and/or Nordic Seas together with decreasing sea level pressure in the Azores and/or southern Europe (Fig. 8b, d, f). The NAO persistently influences the surface temperature and snow cover over the Eurasian continent, sea ice and SST in the North Atlantic from winter to summer[93]. The NAO-induced SST anomalies in the North Atlantic can excite a wave train propagating toward East Asia, which affects the large-scale atmospheric circulation and, thus, regional rainfall pattern[94]. In addition, the negative NAO could weaken the wind-driven AMOC and reduce the poleward ocean heat transport in the North Atlantic[39], further reducing the interhemispheric temperature gradient and the EASM rainfall. However, multiple lines of evidence suggest that the basin-scale AMOC remained fairly stable throughout the Holocene[95]. Therefore, the feedbacks associated with the Holocene AMOC likely play a minor role. In contrast, the Tibetan Plateau, known as the world's third pole with an average elevation of 4000 m, may play a more significant role in shaping the EASM rainfall. The snow-albedo feedback may have amplified the temperature response on the Tibetan Plateau to the end of the Green Sahara. An alkenone-based summer temperature reconstruction from the Qinghai Lake on northeastern Tibetan Plateau indicates a substantial cooling (>5 °C) between 5 and 3.5 ka[96] (Fig. 7d). Since the Tibetan Plateau is the main heat source driving the Asian summer monsoon[97], its abrupt cooling during the end of the Green Sahara could weaken land-sea thermal contrast and greatly reduce the EASM rainfall.

To reveal the spatial pattern of EASM rainfall response to the termination of the Green Sahara, we collect a wealth of hydroclimate records in East Asia based on rigorous criteria (Methods, Supplementary Table 9) and compare them with four climate model simulations (Fig. 9). In addition to our sensitivity experiments conducted with the EC-Earth model[36] (Methods), similar experiments based on the Community Climate System Model version 4 (CCSM4)[98], the water isotope-enabled Community Earth System Model (iCESM)[99], and climate model from the Goddard Institute for Space Studies (GISS)[100] were included for multi-model comparison. Consistent with the proxy records (Supplementary Table 9), nearly all climate models simulate decreasing annual and summer rainfalls in northeastern China, northern China, northeastern Tibetan Plateau, and southwestern China in response to the desertification of the Sahara (Fig. 9). However, the simulated increases in annual and summer rainfalls in southern China contrast with the available proxy records there (Supplementary Table 9 and Fig. 9). Similar to the last deglaciation, we argue that the biases in climate models are likely responsible for this model-proxy discrepancy. We also analyze the changes in autumn rainfall in climate simulations, which show a better agreement with proxy records (Fig. 9). In particular, the EC-Earth and CCSM4 models simulate a widespread autumn drying over the whole East Asia, closely resembling the pattern of proxy records (Fig. 9).

In summary, our quantitative reconstructions of the EASM rainfall amount changes over the past 22,000 years based on multi-methods and multi-proxies provide a benchmark for understanding the forcing and response of EASM rainfall in the context of long-term climate change. Our reconstructions suggest that the EASM rainfall since the LGM is characterized by alternative contrasting stable states and abrupt shifts between these states, indicating a strongly nonlinear nature of the EASM rainfall. In particular, we uncover and define five prominent tipping points in the EASM rainfall, which are linked to abrupt shifts in the AMOC and/or Saharan vegetation cover. In combination with comprehensive paleoclimate data compilations and multi-model simulations, we have drawn a picture of the EASM rainfall responses to abrupt shifts in the AMOC and Saharan vegetation. Our finding that the EASM rainfall was tightly coupled with known tipping elements in the Earth system during the past has practical implications for future change in the EASM rainfall under anthropogenic global warming. The potential "tipping" of tipping elements when global warming exceeds a specific threshold can trigger domino effects on the EASM rainfall and threaten the lives of billions of people.

## Methods

### Site description and modern climate

The Qingtongyang Maar Lake (110°10′E, 20°34′N, elevation 131 m) is located in the Leizhou Peninsula of Guangdong Province, southern China. It is a closed-basin crater lake that has a surface area of 8.81 km$^2$ and a small catchment of 32.13 km$^2$. Because of the small catchment and lack of river input, the lake level is mainly controlled by the rainfall amount falling in the catchment, which makes it an excellent measure of past rainfall changes. Also, this lake lies in the northern boundary of the present-day seasonal ITCZ migration, and thus, the lake status should have been sensitive to past changes in the position of the ITCZ. The surrounding bedrock of this lake is composed of volcanic basalt[101]. No limestone in the catchment minimizes the possibility of introducing old radiocarbon into the lake, which lends credit to $^{14}$C dating and ensures the reliability of age model.

Based on station data available from the China Meteorological Data Service Centre (https://data.cma.cn) during the period 1957–2018 CE (Supplementary Fig. 2), the long-term annual mean temperature (Tann) is 23.3 °C with the mean coldest month (January) temperature of 15.6 °C and the mean warmest month (July) temperature of 28.8 °C. The annual total rainfall (Pann) is 1611 mm, with the driest month (December) rainfall of 24 mm and the wettest month (August) rainfall of 327 mm. The rainy season is from May to October under the influence of the EASM and northward migration of the ITCZ. Since more than 80% of the annual rainfall is contributed by summer rainfall, the variations of annual rainfall are almost identical to that of summer rainfall (Supplementary Fig. 2).

### Drilling and lithology

The sediment cores were recovered from the center of Qingtongyang Maar Lake with piston corer in November 2016. Here we report the upper part of the core, which is coded as QTY-2-1 and spans the last ~22,000 years with firm age control. The lithology of the core is described as follows: 0–5 cm is a surface mixed layer, 5–8 cm is grayish black clay, 8–34.4 cm is grayish brown silty clay, 34.4–73 cm is grayish black clay, 73–82 cm is grayish yellow sandy clay, 82–89 cm is grayish black clay, 89–95.5 cm is grayish yellow sandy clay, 95.5–123 cm is gray-brown yellow sandy clay.

### Dating and chronology

$^{210}$Pb and $^{137}$Cs dating. Samples at 0.5-cm intervals from the top 16 cm of the sediment core were measured for the natural fallout radionuclide $^{210}$Pb and anthropogenic fallout radionuclides $^{137}$Cs. Their activities were measured by the gamma spectrometer using a low-background, hyper-pure germanium detector. Each sample was
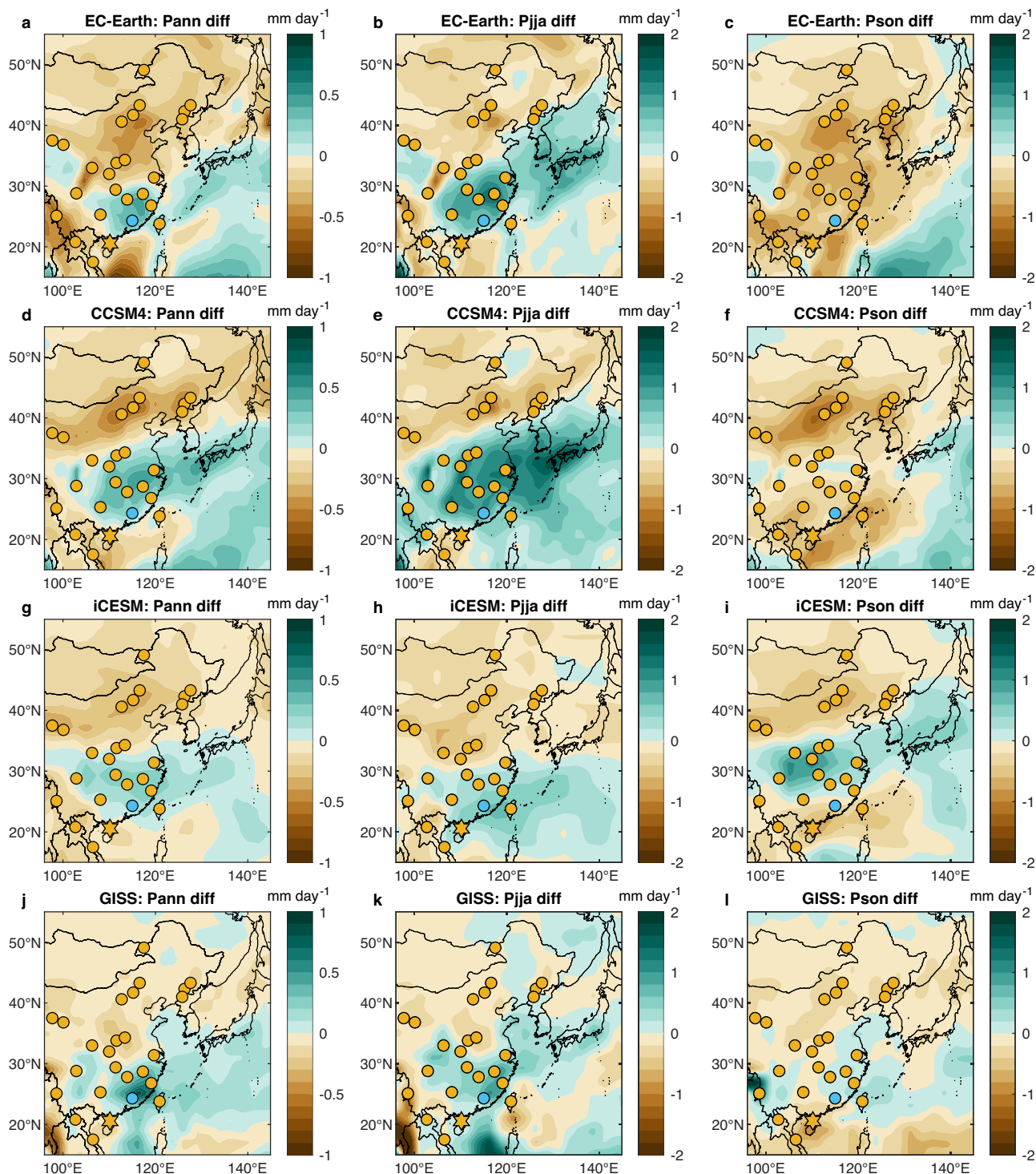
**Fig. 9 | Multi-model simulations showing rainfall response in East Asia to the end of the Green Sahara.** The maps show annual, summer and autumn rainfall differences between the simulations MHORB (mid-Holocene experiment with orbital forcing only) and MHGSRD (mid-Holocene experiment with orbital forcing, a vegetated Sahara and reduced dust emissions) performed with EC-Earth[36] (**a–c**),

CCSM4[98] (**d–f**), iCESM[99] (**g–i**), and GISS[100] (**j–l**), respectively. Pann: annual rainfall; Pjja: summer rainfall; Pson: autumn rainfall. Brown (blue) hexagrams (this study) and circles indicate proxy records with drying (wetting) climate during the mid- to late Holocene transition.

counted for at least 24 h to ensure that both detection limit and measurement error are acceptable. Prior to measurement, samples were freeze-dried, weighed, and stored in sealed containers for 3 weeks to allow for radioactive equilibrium between $^{214}$Pb and its parent radioisotope $^{226}$Ra[102]. The activities of $^{210}$Pb and $^{137}$Cs were determined by gamma emissions at 46.5 and 662 keV, respectively.

$^{226}$Ra activity was measured by the gamma emissions of its daughter radioisotope $^{214}$Pb at 295 and 352 keV. The excess $^{210}$Pb activity ($^{210}$Pb$_{ex}$) was calculated by subtracting the $^{226}$Ra activity from the total $^{210}$Pb activity. Because the sediment was mixed in the top 0–5 cm, we constructed the $^{210}$Pb age model based on the piecewise constant rate of supply (CRS) model[49] constrained by the $^{137}$Cs peak at 1963 CE and two

post-bomb $^{14}$C ages at 1955 CE and 2014 CE (Supplementary Fig. 6), which was implemented in the R package 'serac'[103].

**AMS $^{14}$C dating.** Sixteen charcoal samples from various depths of the sediment core were collected for AMS (accelerator mass spectrometry) $^{14}$C dating (Supplementary Table 1). Samples were chemically pretreated using standard acid-alkali-acid method[104] and graphitized on a fully automated system[105]. $^{14}$C content was measured on the MICADAS system[106] in the AMS laboratory of Nanjing University[107]. The positive $^{14}$C dates were calibrated to calendar years before present (BP), where present refers to 1950 CE, based on the IntCal20 curve[108]. The negative $^{14}$C dates were calibrated using monthly data of the Northern Hemisphere post-bomb calibration curve 3[109]. Calibrations were implemented in the software OxCal[110]. For stability, the $^{14}$C age model is based on linear interpolation and extrapolation of the median values of the calibrated $^{14}$C dates, with two outliers excluded (Supplementary Fig. 5). According to the age model, the bottom of core QTY-2-1 is estimated to be 22,680 yr BP, but we limit our analysis to the last 22,000 years to account for potential disturbances at the core's end during drilling.

## Core scanning and calibration

The color of sediment is an indicator of sediment composition changes and has been used successfully as a proxy for paleomonsoon precipitation changes[111–115]. Digital images of the sediment core surface were taken by a high-resolution line scan camera installed in the Geotech MSCL-XRF core scanner. Sediment color b*, representing the blue (negative) to yellow (positive) component, was extracted from digital images in a rectangle along the core direction with a width of ~15 mm and at an unprecedented sampling interval of 100 μm, yielding an overall temporal resolution of ~1 years and 0.1-year resolution in the period overlapping with instrumental records.

Continuous and non-destructive X-ray fluorescence (XRF) element scanning was carried out at 1 mm resolution on the split sediment cores, corresponding to an overall sampling resolution of ~10 years and 1-year resolution in the period overlapping with instrumental records. The sediment core surfaces were covered with a 4 μm-thick thin film to avoid contamination of the scanning instruments. All XRF scanning measurements were conducted with a generator setting of 10 KV and a sampling time of 20 s. The irradiated dimensions of the core surface are $15 \times 1$ mm$^2$. The split sediment cores were freeze-dried before scanning to avoid the influence of water content on the results of XRF[116]. The geochemical elements were calibrated using the immobile element titanium (Ti) to isolate the proportion of changes associated with climate:

$$X_{calib} = X_{raw} \times \frac{X_{raw} - Ti}{X_{raw} + Ti} \qquad (1)$$

In Eq. (1), $X_{raw}$ represents the raw value and $X_{calib}$ represents the calibrated value. From a physical and chemical perspective, $X_{calib}$ represents the proportion of element change attributable to redox conditions and/or salinity. A similar process was used to quantify the near-infrared reflectance of terrestrial vegetation based on satellite remote sensing[117]. This equation is a nonlinear transform of the element ratio ($X_{raw}$/Ti), which is insensitive to dilution effects and can accommodate the inherent non-linearity of the relation between element intensity and concentration[118]. As a ratio, it has the advantage of minimizing some element-correlated noise and influences attributable to variations in direct/diffuse irradiance, surface morphology, and atmospheric attenuation[116,118,119]. To a lesser degree, the ratio can reduce instrument-related errors[119]. The distribution of iron after calibration was still highly skewed and it was further logarithmically transformed to make its response to climate more linearly.

## Rainfall reconstruction

**Instrumental target.** Our reconstruction target is annual rainfall based on the calendar year that covers a full cycle of the rainy season. Monthly rainfall deviations from the climatological mean (1961–1990 CE) of three meteorological stations surrounding the Qingtongyang Maar Lake were averaged to represent regional rainfall variability (Supplementary Fig. 2). The stations from Hainan Island were not included because rainfall variability on Hainan Island is poorly correlated with that of the Leizhou Peninsula. Climate data were downloaded from the China Meteorological Data Service Centre (https://data.cma.cn). The period 1953–2005 CE were used for calibration because of the least missing values and overlapping with proxy data. The period prior to 1953 CE was not used for calibration because of large uncertainty in the climate data. Missing climate values were filled in using the regularized expectation maximization (RegEM) algorithm[120] with truncated total least squares regression[121]. Grided rainfall data from the Global Precipitation Climatology Centre (GPCC) version 2022[44] were used as an additional independent validation of our reconstructions. To preserve the full amplitude of climate variability and avoid spurious signals, both climate data and proxy records were decadally smoothed with a cubic-smoothing spline[45] to have roughly the same frequency (Supplementary Fig. 3), following the suggestion of previous studies[46–48]. Since smoothing can influence the degrees of freedom (DOF), we assumed DOF = 51 for the raw data, which has an effective sample size (ESS) of 53 years, and DOF = 3 for the smoothed data, which has an ESS of five decades[47].

**Proxy data.** Proxy data measured on core QTY-2-1 from the Qingtongyang Maar Lake were used as predictors for rainfall reconstruction, including color b* and elemental concentrations of iron, manganese, and calcium. These proxy records are sensitive to redox conditions and/or salinity in the lake which are controlled by regional rainfall (Supplementary Discussion). We decided to choose these four proxy records based on three criteria. Firstly, from the statistical perspective, there should be a significant correlation ($P < 0.02$) between proxy and climate targets in their common time period. We utilized both correlation and partial correlation to analyze the relationship between our proxies and climate data, which shows that rainfall is the dominant controlling factor of changes in these proxy records (Supplementary Table 2). The impact of smoothing on the degrees of freedom was considered during statistical analysis. Secondly, from the physical and chemical perspective, the qualitative relationship between proxies and climate can be explained and the mechanisms have been relatively well recognized (Supplementary Discussion). Lastly, the temporal resolution of proxy records should be at least one year or finer during the calibration period to facilitate meaningful calibration with rainfall observations. To evaluate the common variance of proxy records and the stability of climate-proxy relationships over time, we calculated the running expressed population signal (EPS)[53] and mean inter-series correlation (Rbar)[53] using a sliding window of 3000 years (Fig. 2e).

**Ensemble parameters.** To address various sources of uncertainty, 1650 members of reconstructions were obtained for each reconstruction method by perturbing the following parameters:

(1) 0–25% of proxy records were randomly removed before reconstruction to test for the robustness of proxy selection[122].

(2) To overcome bias in the choice of calibration period[46] whilst retaining the autocorrelation structure[123], all possible combinations of 5-year blocks and additional successive years with a length of 33/38 years were used for training, while the remaining 20/15 years were used for validation.

(3) Gaussian noises with standard deviations equal to measurement errors were added to the proxy data to simulate the influence of measurement uncertainties. This treatment can improve the generalization of the reconstruction model and avoid overfitting.

(4) The weight of each proxy is multiplied by a random scalar drawn from a uniform distribution in the interval between 1/1.5 and 1.5[124]. This treatment simulates the influence of proxy weights[122] and age model uncertainties (Supplementary Fig. 4). Before weighting, all proxy records were normalized to have zero mean and standard deviation units over the calibration period.

(5) Red noise with its standard deviation equal to the root mean square error (RMSE) and its first-order autoregression (AR1) coefficient identical to that of regression residual was added to the result to represent the unexplained variance.

**Composite plus scale (CPS).** CPS is a classical method for quantitative climate index reconstruction and has been widely used to reconstruct mean climate of various spatial scale[47,125,126]. The proxy matrix is normalized over the calibration period and weighted averaged to form a single time series, which is then scaled to have the same mean and standard deviation as the reconstruction target. Here we perform CPS in a way similar to previous studies[122,124]: the normalized proxies were weighted by their non-detrended correlation with rainfall observation over the calibration period. Like many linear methods, CPS is prone to variance losses and the reconstructions tend to be biased toward zero, which are directly related to the correlation between proxies and the climate target[127]. CPS is computationally efficient, and its performance is often comparable to that of more complicated methods (Supplementary Fig. 7).

**Principal component regression (PCR).** PCR is a popular method commonly used in both climate index and climate field reconstructions[47,122,124,128–130]. PCR reduces the dimension of the proxy matrix by principal component analysis (PCA) and only retains the first few principal components (PC) as predictors in the regression. All PCs are linear combinations of the original proxies and orthogonal to each other, which copes well with the problem of multicollinearity. Here we perform PCA over the calibration period using the singular value decomposition (SVD) algorithm[131], retaining the first few PCs that explain up to 95% of the total variance to reduce noise. If PC1 explains more than 95% of the total variance, we retain only PC1. The number of retained PCs was selected in such a way because there exist many methods to truncate PCs without an objectively discernible best method, and the truncation is sensitive to the period over which the PCA is performed[125].

**Partial least squares (PLS).** Though PLS regression is a basic tool widely used in chemometrics[132], it is less seen in tree-ring-based climate reconstructions compared to CPS and PCR, except in some pollen- and diatom-based quantitative reconstructions[133]. PLS regression is of particular interest because it has the ability to analyze data with numerous noisy and collinear variables in two data matrices, X and Y[132]. Similar to the PCR method, PLS constructs components as linear combinations of the original predictor variables but has more advantages. In contrary to PCR, which constructs components to maximize the explained variance of predictors, PLS finds components that have a large covariance with the response variables. Therefore, PLS regression can achieve a parsimonious model with reliable predictive power. Here, we perform PLS regression using the SIMPLS algorithm[134] and select the optimal number of PLS component based on two-sample $t$-test ($P < 0.01$)[135] and require a reduction of RMSE in the validation period by at least 5%[136].

**Optimal information extraction (OIE).** The OIE method is a variant of the CPS method, which integrates the features of local (LOC) method[137], a Bayesian framework[138], the generalized likelihood uncertainty estimation (GLUE)[139,140], and ensemble reconstruction[46,122]. This method has the advantage of efficiently extracting low-frequency climate signals, since it accounts for the nonlinear response of proxy to

climate based on Bayesian theory[141]. Instead of variance matching in the CPS, the OIE sets the prior distribution of regression coefficients as a uniform distribution in the ranges between direct and indirect regressions, and the posterior distribution is determined by the GLUE method[139,140]. Here we run the Markov Chain Monte Carlo (MCMC) simulation in the GLUE using the Metropolis–Hastings algorithm[142] and calculate the acceptance probability of regression coefficients based on the RMSE of the validation period[143]. The MCMC sampling process generates 1000 realizations of reconstruction and the median is used as one of the ensemble members.

**Point-by-point regression (PPR).** PPR is a well-tested and easily interpreted PCR method that has been applied to create high-quality drought atlases worldwide[129,144]. PPR assumes that only those proxy records located relatively close to a given point are likely to be true predictors of climate at that location, where "true" indicates a causal relationship between proxy and climate that is stable through time. The PPR is initially designed for climate field reconstruction but can also be used for climate index reconstruction. Unlike PCR, which performs PCA over the calibration period, the PPR performs PCA over the whole period of proxy records and puts the orthogonal PCs into stepwise regression by the order of explanatory variance, which can avoid the insufficient representativeness of a short calibration period and extract the common variability linked to climate change. Here we determine the optimum number of PCs put into regression model based on two-sample $t$-test[135] and a threshold of at least 5% reduction in the RMSE in the validation period[136].

**Ridge regression (RIG).** Ridge regression is an approach for determining the coefficients of a linear model that contains linearly correlated predictors[145]. Estimations of coefficients for multiple linear regression models rely on the independence of model terms. However, when terms are correlated, and the columns of predictor matrix X have an approximate linear dependence, the matrix $(X^TX)^{-1}$ is close to singular. As a result, the least squares estimate is sensitive to random errors in the response variable Y, producing large variance, which is called multicollinearity. Ridge regression resolves the problem of multicollinearity by estimating regression coefficients using $\beta = (X^TX + kZ)^{-1}X^TY$, where k is the ridge parameter, and Z is the identity matrix. Small, positive values of k improve the conditioning of the problem and reduce the variance of the estimates. While biased, the reduced variance of ridge estimates often results in a smaller mean squared error when compared to least squares estimates. Here, we set k as a random scalar evenly distributed in the range from 0 to 100, and its final distribution is determined using the GLUE method[139,140] and other details on the MCMC sampling are identical to that of the OIE method.

**Lasso and elastic net (ELN).** Similar to the ridge regression, the lasso is a regularization method for performing linear regression[146]. However, lasso is a shrinkage estimator which includes a penalty term constraining the size of the estimated coefficients and thus forcing some coefficients to be zero. As the penalty term increases, lasso lets more coefficients to be zero. Elastic net is a hybrid of ridge regression and lasso regularization[147]. Like lasso, elastic net can generate reduced models by generating zero-valued coefficients, but it outperforms lasso on data with highly correlated predictors. Here, we perform elastic net by setting the weight of lasso versus ridge optimization as 0.5, and the regularization coefficient 'lambda' is determined by tenfold cross-validation and equals the maximum "lambda" value such that the RMSE is within one standard error of the minimum cross-validation error.

**Artificial neural network (ANN).** ANN is a machine learning method that imitates biological neural network, a part of artificial intelligence technology[148,149]. It has the ability to learn and make inferences from

data, mimicking the way that the brain processes information. ANN model consists of a series of layers, namely the input, hidden, and output layers. The first hidden layer has connections from input data, and each subsequent layer has connections from the previous layer. Each layer multiplies the input by a weight matrix and adds a bias vector. An activation function follows each hidden layer. The last layer produces the network's output, namely predicted values. ANN with only one hidden layer can solve any problem of finite input-output mapping, given enough neurons in the hidden layer. The model used here is a fully connected feedforward backpropagation ANN with three hidden layers containing 100, 25, and 10 neurons, respectively. The linear transfer function is used. Data from the validation period are used to monitor training convergence every ten iterations.

**Convolutional neural network (CNN).** CNN is a deep learning method designed to process data in the form of multiple arrays[150]. CNN is commonly applied in tasks such as image detection, recognition, and classification, but can also be used for regression problems[151]. It is the convolutional layer and pooling layer that make CNN unique. Our CNN consists of seven layers in order: a sequence input layer, a one-dimensional (1D) convolutional layer with filter size of 3 and neurons of 32, a batch normalization layer to speed up training and reduce the sensitivity to model initialization[152], a 1D average pooling layer with pool size equal to filter size, a Monte Carlo dropout layer with dropping probability of 50% to prevent the model from overfitting[153], and a fully connected layer followed by a regression output layer. The weights of the model are initialized with the He initializer, which samples from a normal distribution with zero mean and variance of 2 divided by input size[154]. Padding was conducted so that the output has the same size as the input and reduces the influence of the edge effect. Data augmentation was performed by adding Gaussian noise to the input data to make the model more stable and avoid overfitting[155]. The model was trained with the Adam optimizer with a maximum epoch of 100, minimum batch size of 20%, and initial learning rate of 0.01. Gradient clipping was applied to prevent gradient exploding. Furthermore, we conducted independent validation every ten iterations and stop the training early with a patience of five epochs, which is another regularization method to prevent overfitting. The validation data was shuffled before each validation.

**Verification statistics.** We use four verification statistics to assess the reliability of the reconstruction models. These statistics evaluate the ability of the proxy to reconstruct climate over verification periods that are independent of calibration periods. (i) Pearson correlation coefficient (R), a powerful statistic for testing the relative association between two variables. (ii) Reduction of error (RE), which determines if a reconstruction is better than climatology, i.e., the mean of rainfall in the calibration period. There are no formal statistical significance tests for RE, but a RE >0 indicates that the reconstruction is better than using the mean of the calibration period as forecast. RE is a rigorous verification statistic because it has no lower boundary. (iii) Coefficient of efficiency (CE). Like RE, there are no formal statistical significance test for CE, but a CE >0 indicates that the reconstruction is better than using the mean of the verification period as forecast. CE is more rigorous than RE[129]. (iv) Root mean square error (RMSE), which measures the average difference between the reconstructed and observed rainfall.

**Compilation of East Asian hydroclimate records**
To test the robustness of abrupt shifts in East Asian hydroclimate, we compile proxy records from various climatic zones based on rigorous criteria: (i) Reflect local and/or regional summer hydroclimate changes. Because the climatic interpretation of speleothem $\delta^{18}O$ records in East Asia remains controversial[13], we only include the speleothem $\delta^{18}O$ records that have been linked to hydroclimate change based on

correlation with instrumental records and/or independent rainfall-related proxy records such as $\delta^{13}C$ records. (ii) The proxy records should at least cover the transition period from middle to late Holocene at 5–3 ka BP and/or one of the millennial-scale events during the last deglaciation (HS1, BA, YD) without hiatus longer than 500 years. (iii) The standard errors of age-control points should be less than 100 years in most cases and no larger than 800 years. (iv) At least three age-control points span or closely bracket the period of interest. The gap between successive ages should be smaller than 3000 years for the period 18–11 ka BP, and there should be at least one age-control point within the period 3.5–4.5 ka BP. (v) Has a mean resolution finer than 200 years. But this was relaxed to 300 years for regions where proxy records are scarce and 500 years for the lake level records. Details of the compiled proxy records are listed in Supplementary Tables 5–9 and some records are shown in Supplementary Figs. 12, 13. Most records are not continuous over the past 22,000 years and the source data are not publicly available. Therefore, it is impossible to make a continuous composite time series to describe the evolution of the East Asian hydroclimate since the LGM. However, these records can provide insights into hydroclimate changes during specific abrupt climate events, which were compared with model simulations.

**Synthesis of African summer monsoon**
A total of six $dD_{wax}$ records (Supplementary Table 10) were combined into a composite time series to characterize the evolution of the African summer monsoon, encompassing both the West African and East African monsoons, during the Holocene. The proxy records were selected based on these criteria: (i) Reflect local and/or regional summer hydroclimate rather than winter, excluding proxy records from areas currently influenced by the Mediterranean climate. (ii) Span a minimum duration of 9000 years with no recorded hiatus during the period 11–0 ka BP. (iii) There should be at least one age-control point every 3000-year interval. (iv) Has a median resolution finer than 300 years in the period 6–2 ka BP; (v) Both the sampling depths and proxy data are publicly available for reanalysis of the age model.

There are two main sources of uncertainty in the paleoclimate data, i.e., proxy measurement uncertainty and age model uncertainty[156]. We generated 10,000 age models using the R package 'rbacon'[157] for each record and perturbed the proxy by adding random noise drawing from a normal distribution with a standard deviation equal to the measurement error. Then the perturbed proxy records were interpolated against the perturbed age models at 10-year resolution using the shape-preserving piecewise cubic interpolation method. Prior to calculating the composite mean, the interpolated $dD_{wax}$ records were corrected for ice volume change[158] and subtracted by the mean and divided by the standard deviation during the period 12–2 ka BP that is common to all records to form a standardized time series. Furthermore, the standardized time series were multiplied by −1 so that greater proxy values indicate higher rainfall amounts.

**Detection of abrupt shifts and their timings**
Three different methods were applied to detect abrupt shifts associated with tipping points in the proxy records, including the regime shift analysis[54,55], Bayesian change-point analysis[56], and the rate of change. Regime shifts are defined as rapid reorganizations of a system from one relatively stable state to another[54]. The regime shift analysis[54,55] splits a time series into multiple segments with significantly different mean and identifies the point at which abrupt changes in the mean occur. Regime shift analysis was performed using the function "ischange" in the software MATLAB with the maximum number of change points set to 5 for the past 22,000 years. To validate the results of regime shift analysis, a Bayesian ensemble algorithm[56] was independently used to detect abrupt shifts in the proxy records. Unlike conventional criterion-based methods that select a single best model, the Bayesian paradigm embraces all candidate models, evaluates their

probabilities, and synthesizes them into an average model[56]. These two independent methods perform well in detecting abrupt shifts in our rainfall reconstruction and show consistent results (Supplementary Fig. 10). Once the timings of abrupt shifts in our rainfall reconstruction were determined, the corresponding depths were calculated, and Bayesian age modeling[157] was employed to assess age uncertainties. However, for low-resolution records, the timings of abrupt shifts may not align well with those detected by these two methods. In this case, the rate of change was used to determine the precise timings of abrupt shifts. The rate of change in the composite time series of the African summer monsoon was calculated, and the period with the rate of change exceeding two standard deviations of the period 11–0 ka BP was considered as the range of abrupt change in the time series (Supplementary Fig. 16). Since the composite time series of the African summer monsoon has been smoothed by averaging different realizations of uncertainties in both proxy measurement and age model, no additional smoothing was applied. The rate of change was not applied to detect abrupt changes in our rainfall reconstruction because the changes in ultra-high-resolution records are very abrupt, and the selection of smoothing parameters, such as window length, is quite subjective and cannot adapt universally to abrupt events with different amplitudes.

## Climate model simulations

**TRACE-21ka and iTRACE**. To reveal the spatial pattern of rainfall response in East Asia to abrupt shifts in the AMOC during the last deglaciation, we compare our rainfall reconstruction and the proxy records we compiled with model results from two transient climate experiments, i.e., the TRACE-21ka[71] and iTRACE[16]. The TRACE-21ka simulated continuous climate evolution of the last 21,000 years using the Community Climate System Model version 3 (CCSM3) with a spatial resolution of T31 (3.75°)[71]. The transient climate forcings include orbitally-induced solar insolation variations[159], atmospheric greenhouse gas concentrations[160], meltwater fluxes[71], and continental ice sheets[161]. The iTRACE was performed in the state-of-the-art water isotope-enabled version of the Community Earth System Model version 1.3 (iCESM1.3)[16], which largely follows the strategy of the TRACE-21ka[71]. The iCESM1.3[162] is composed of the Community Atmosphere Model (CAM5.3), Parallel Ocean Program (POP2), Los Alamos Sea Ice Model (CICE4), and Community Land Model (CLM4). The spatial resolution of atmosphere and land is 1.9° in latitude and 2.5° in longitude, with 30 vertical levels in the atmosphere. The horizontal resolution of ocean and sea ice is nominal 1° (gx1v6), with 60 vertical levels in the ocean.

All experiments in the iTRACE were integrated from the LGM (20 ka) to the early Holocene (11 ka). Three parallel transient sensitivity experiments (ICE, ICE + ORB, and ICE + ORB + GHG) were performed with three climatic forcing added one by one, i.e., the ice sheet (ICE-6G)[163], the orbital forcing[159], and the greenhouse gas forcing[160]. The baseline iTRACE simulation (i.e., ICE + ORB + GHG + MWF) was branched from the ICE + ORB + GHG run at 19 ka, with the imposed meltwater forcing (MWF) similar to that in the TRACE-21ka[71]. The ice sheet in the iTRACE was changed every thousand years from 19 ka to 11 ka. The ocean bathymetry was modified twice at 14 ka and 12 ka based on the ICE-6G reconstruction[163].

**Green Sahara experiments**. The Green Sahara sensitivity experiments were performed using the European Community Earth System Model (EC-Earth) version 3.1[164]. The EC-Earth is a fully coupled Earth system model that includes several state-of-the-art components to describe the atmosphere, ocean, sea ice, land surface, dynamic vegetation, atmospheric composition, ocean biogeochemistry, and the Greenland Ice Sheet[165]. The atmospheric component is based on the Integrated Forecasting System (IFS cycle 36r4) of the European Centre for Medium-Range Weather Forecasts with a horizontal resolution of T159

(1.125°) and 62 vertical levels. The ocean component is based on the Nucleus for European Modeling of the Ocean (NEMO), which uses a tripolar grid with a horizontal resolution of 1° and 46 vertical levels. The EC-Earth has proven its success in simulating the Earth's climate across past and future scenarios[165,166]. It shows good skills in capturing the nuanced spatial and temporal patterns of monsoon rainfall in present-day climate[36,167].

To understand the response of rainfall in East Asia to the changes in Saharan vegetation during the end of the Green Sahara, we performed two sets of mid-Holocene (MH) experiments: one control experiment driven by orbital forcing only (MHORB), and an idealized experiment (MHGSRD) incorporating both orbital forcing and a vegetated Sahara with reduced dust emissions. The MHORB experiment was performed following the protocol of the Paleoclimate Modeling Intercomparison Project phase 3 (PMIP3)[168] with orbital parameters fixed at 6 ka[169]. The concentrations of atmospheric $CO_2$, $CH_4$, and $N_2O$ were fixed at the preindustrial level, i.e., 280 ppm, 650 ppb, and 270 ppb, respectively. Other boundary conditions, such as land-sea distributions, ice sheets, topography, vegetation cover, and dust emission were the same as the preindustrial period. In the MHGSRD experiment, the vegetation type over the Sahara region (11°N–33°N and 15°W–35°E) was modified to shrub, and the dust emission from the Sahara Desert was reduced by 80%[36] according to the proxy-based estimation of Saharan dust flux reduction during the mid-Holocene[34,170]. The change of vegetation cover from desert (MHORB) to shrub (MHGSRD) corresponds to a decrease in surface albedo from 0.3 to 0.15 and an increase in the leaf area index from 0.2 to 2.6[36]. The dust reduction from the MHORB to the MHGSRD led to a decrease in the global dust aerosol optical depth (AOD) by about 60% and a total AOD of 0.02[36]. Such changes in vegetation cover and dust emissions were not intended to precisely replicate mid-Holocene Saharan conditions but were designed to provide insights into their potential climate feedback.

## Data availability

The proxy data and climate reconstructions generated in this study are provided in the Supplementary Information and Source Data file. The model data presented in this study are available in Zenodo at https://zenodo.org/records/14257821. Source data are provided with this paper.

## Code availability

The R package "rbacon" is available at https://cran.r-project.org/web/packages/rbacon/index.html. The R package "serac" is available on GitHub at https://github.com/rosalieb/serac. The code for Bayesian change-point analysis is available on GitHub at https://github.com/zhaokg/Rbeast. The reduced chi-square test was performed with the IsoplotR toolbox available at https://www.ucl.ac.uk/~ucfbpve/isoplotr/home/. Our rainfall reconstructions were performed in the commercial software MATLAB version R2023b using the Deep Learning Toolbox and the Statistics and Machine Learning Toolbox.

## References

1. Lenton, T. M. et al. Tipping elements in the Earth's climate system. *Proc. Natl Acad. Sci. USA* **105**, 1786–1793 (2008).
2. Lenton, T. M. et al. Climate tipping points — too risky to bet against. *Nature* **575**, 592–595 (2019).
3. Armstrong McKay, D. I. et al. Exceeding 1.5 °C global warming could trigger multiple climate tipping points. *Science* **377**, eabn7950 (2022).
4. Cai, Y., Lenton, T. M. & Lontzek, T. S. Risk of multiple interacting tipping points should encourage rapid $CO_2$ emission reduction. *Nat. Clim. Change* **6**, 520–525 (2016).
5. Rocha, J. C., Peterson, G., Bodin, Ö. & Levin, S. Cascading regime shifts within and across scales. *Science* **362**, 1379–1383 (2018).

6. Klose, A. K., Wunderling, N., Winkelmann, R. & Donges, J. F. What do we mean, 'tipping cascade'? *Environ. Res. Lett.* **16**, 125011 (2021).

7. Liu, T. et al. Teleconnections among tipping elements in the Earth system. *Nat. Clim. Change* **13**, 67–74 (2023).

8. Barnosky, A. D. et al. Approaching a state shift in Earth's biosphere. *Nature* **486**, 52–58 (2012).

9. Steffen, W. et al. Trajectories of the Earth System in the Anthropocene. *Proc. Natl Acad. Sci. USA* **115**, 8252–8259 (2018).

10. Douville, H. et al. in *Climate Change 2021: The Physical Science Basis. Contribution of Working Group I to the Sixth Assessment Report of the Intergovernmental Panel on Climate Change* (eds Masson-Delmotte, V. et al.) (Cambridge Univ. Press, 2021).

11. Brovkin, V. et al. Past abrupt changes, tipping points and cascading impacts in the Earth system. *Nat. Geosci.* **14**, 550–558 (2021).

12. Allen, M. R. & Ingram, W. J. Constraints on future changes in climate and the hydrologic cycle. *Nature* **419**, 228–232 (2002).

13. Cheng, H. et al. The Asian monsoon over the past 640,000 years and ice age terminations. *Nature* **534**, 640–646 (2016).

14. Pausata, F. S. R., Battisti, D. S., Nisancioglu, K. H. & Bitz, C. M. Chinese stalagmite δ¹⁸O controlled by changes in the Indian monsoon during a simulated Heinrich event. *Nat. Geosci.* **4**, 474–480 (2011).

15. Zhang, H. et al. East Asian hydroclimate modulated by the position of the westerlies during Termination I. *Science* **362**, 580 (2018).

16. He, C. et al. Hydroclimate footprint of pan-Asian monsoon water isotope during the last deglaciation. *Sci. Adv.* **7**, eabe2611 (2021).

17. Hu, C. et al. Adsorbed silica in stalagmite carbonate and its relationship to past rainfall. *Geochim. Cosmochim. Acta* **69**, 2285–2292 (2005).

18. Wang, Q. et al. Orbital- and millennial-scale hydroclimate changes in central China during the last glacial period. *Quat. Sci. Rev.* **337**, 108802 (2024).

19. Han, Z. et al. Extreme monsoon aridity episodes recorded in South China during Heinrich events. *Palaeogeogr. Palaeoclimatol. Palaeoecol.* **440**, 467–474 (2015).

20. Zhou, X. et al. Catastrophic drought in East Asian monsoon region during Heinrich event 1. *Quat. Sci. Rev.* **141**, 1–8 (2016).

21. Zhang, W., Wang, Y., Wu, J. & Duan, F. Last deglacial climate variations inferred from trace elements in a stalagmite from Hulu Cave. *Nanjing Quat. Sci.* **34**, 1227–1237 (2014).

22. Wunderling, N. et al. Climate tipping point interactions and cascades: a review. *Earth Syst. Dynam.* **15**, 41–74 (2024).

23. Wang, S. et al. Mechanisms and impacts of Earth system tipping elements. *Rev. Geophys.* **61**, e2021RG000757 (2023).

24. Srokosz, M. A. & Bryden, H. L. Observing the Atlantic meridional overturning circulation yields a decade of inevitable surprises. *Science* **348**, 1255575 (2015).

25. Frierson, D. M. W. et al. Contribution of ocean overturning circulation to tropical rainfall peak in the Northern Hemisphere. *Nat. Geosci.* **6**, 940–944 (2013).

26. Schneider, T., Bischoff, T. & Haug, G. H. Migrations and dynamics of the intertropical convergence zone. *Nature* **513**, 45–53 (2014).

27. Smeed, D. A. et al. The North Atlantic Ocean is in a state of reduced overturning. *Geophys. Res. Lett.* **45**, 1527–1533 (2018).

28. Caesar, L., Rahmstorf, S., Robinson, A., Feulner, G. & Saba, V. Observed fingerprint of a weakening Atlantic Ocean overturning circulation. *Nature* **556**, 191–196 (2018).

29. Weijer, W., Cheng, W., Garuba, O. A., Hu, A. & Nadiga, B. T. CMIP6 models predict significant 21st century decline of the Atlantic meridional overturning circulation. *Geophys. Res. Lett.* **47**, e2019GL086075 (2020).

30. Ditlevsen, P. & Ditlevsen, S. Warning of a forthcoming collapse of the Atlantic meridional overturning circulation. *Nat. Commun.* **14**, 4254 (2023).

31. Boers, N. Observation-based early-warning signals for a collapse of the Atlantic meridional overturning circulation. *Nat. Clim. Change* **11**, 680–688 (2021).

32. Clark, P. U. et al. Global climate evolution during the last deglaciation. *Proc. Natl Acad. Sci. USA* **109**, E1134–E1142 (2012).

33. Evan, A. T., Flamant, C., Gaetani, M. & Guichard, F. The past, present and future of African dust. *Nature* **531**, 493–495 (2016).

34. deMenocal, P. et al. Abrupt onset and termination of the African Humid Period: rapid climate responses to gradual insolation forcing. *Quat. Sci. Rev.* **19**, 347–361 (2000).

35. Tierney, J. E. & deMenocal, P. B. Abrupt shifts in Horn of Africa hydroclimate since the Last Glacial Maximum. *Science* **342**, 843–846 (2013).

36. Pausata, F. S. R., Messori, G. & Zhang, Q. Impacts of dust reduction on the northward expansion of the African monsoon during the Green Sahara period. *Earth Planet. Sci. Lett.* **434**, 298–307 (2016).

37. Pausata, F. S. R. et al. Greening of the Sahara suppressed ENSO activity during the mid-Holocene. *Nat. Commun.* **8**, 16020 (2017).

38. Pausata, F. S. R. et al. Tropical cyclone activity enhanced by Sahara greening and reduced dust emissions during the African Humid Period. *Proc. Natl Acad. Sci. USA* **114**, 6221–6226 (2017).

39. Muschitiello, F., Zhang, Q., Sundqvist, H. S., Davies, F. J. & Renssen, H. Arctic climate response to the termination of the African Humid Period. *Quat. Sci. Rev.* **125**, 91–97 (2015).

40. Sun, W. et al. Northern Hemisphere land monsoon precipitation increased by the Green Sahara during middle Holocene. *Geophys. Res. Lett.* **46**, 9870–9879 (2019).

41. Griffiths, M. L. et al. End of Green Sahara amplified mid- to late Holocene megadroughts in mainland Southeast Asia. *Nat. Commun.* **11**, 4204 (2020).

42. Wang, J., Emile-Geay, J., Guillot, D., McKay, N. P. & Rajaratnam, B. Fragility of reconstructed temperature patterns over the Common Era: implications for model evaluation. *Geophys. Res. Lett.* **42**, 7162–7170 (2015).

43. Büntgen, U. et al. The influence of decision-making in tree ring-based climate reconstructions. *Nat. Commun.* **12**, 3411 (2021).

44. Becker, A. et al. A description of the global land-surface precipitation data products of the Global Precipitation Climatology Centre with sample applications including centennial (trend) analysis from 1901-present. *Earth Syst. Sci. Data* **5**, 71–99 (2013).

45. Cook, E. & Peters, K. The smoothing spline: a new approach to standardizing forest interior tree-ring width series for dendroclimatic studies. *Tree-Ring Bull.* **41**, 45–53 (1981).

46. Frank, D. C. et al. Ensemble reconstruction constraints on the global carbon cycle sensitivity to climate. *Nature* **463**, 527–530 (2010).

47. Mann, M. E. et al. Proxy-based reconstructions of hemispheric and global surface temperature variations over the past two millennia. *Proc. Natl Acad. Sci. USA* **105**, 13252–13257 (2008).

48. Moberg, A., Sonechkin, D. M., Holmgren, K., Datsenko, N. M. & Karlén, W. Highly variable Northern Hemisphere temperatures reconstructed from low- and high-resolution proxy data. *Nature* **433**, 613–617 (2005).

49. Appleby, P. G. & Oldfield, F. The calculation of lead-210 dates assuming a constant rate of supply of unsupported ²¹⁰Pb to the sediment. *Catena* **5**, 1–8 (1978).

50. Barron, V. & Torrent, J. Use of the Kubelka-Munk theory to study the influence of iron oxides on soil colour. *J. Soil Sci.* **37**, 499–510 (1986).

51. Davison, W. Iron and manganese in lakes. *Earth Sci. Rev.* **34**, 119–163 (1993).

52. Liu, X., Colman, S. M., Brown, E. T., Minor, E. C. & Li, H. Estimation of carbonate, total organic carbon, and biogenic silica content by FTIR and XRF techniques in lacustrine sediments. *J. Paleolimnol.* **50**, 387–398 (2013).

53. Wigley, T. M. L., Briffa, K. R. & Jones, P. D. On the average value of correlated time series, with applications in dendroclimatology and hydrometeorology. *J. Appl. Meteorol. Climatol.* **23**, 201–213 (1984).

54. Rodionov, S. N. A sequential algorithm for testing climate regime shifts. *Geophys. Res. Lett.* **31** (2004).

55. Killick, R., Fearnhead, P. & Eckley, I. A. Optimal detection of changepoints with a linear computational cost. *J. Am. Stat. Assoc.* **107**, 1590–1598 (2012).

56. Zhao, K. et al. Detecting change-point, trend, and seasonality in satellite time series data to track abrupt changes and nonlinear dynamics: a Bayesian ensemble algorithm. *Remote Sens. Environ.* **232**, 111181 (2019).

57. Xiao, J. et al. The 4.2 ka event and its resulting cultural interruption in the Daihai Lake basin at the East Asian summer monsoon margin. *Quat. Int.* **527**, 87–93 (2019).

58. Liu, Z. et al. Chinese cave records and the East Asia summer monsoon. *Quat. Sci. Rev.* **83**, 115–128 (2014).

59. Wang, B., Jin, C. & Liu, J. Understanding future change of global monsoons projected by CMIP6 models. *J. Clim.* **33**, 6471–6489 (2020).

60. Tierney, J. E. et al. Glacial cooling and climate sensitivity revisited. *Nature* **584**, 569–573 (2020).

61. Shakun, J. D. et al. Global warming preceded by increasing carbon dioxide concentrations during the last deglaciation. *Nature* **484**, 49–54 (2012).

62. Osman, M. B. et al. Globally resolved surface temperatures since the Last Glacial Maximum. *Nature* **599**, 239–244 (2021).

63. Marcott, S. A. et al. Centennial-scale changes in the global carbon cycle during the last deglaciation. *Nature* **514**, 616–619 (2014).

64. Berger, A. & Loutre, M. F. Insolation values for the climate of the last 10 million years. *Quat. Sci. Rev.* **10**, 297–317 (1991).

65. McManus, J. F., Francois, R., Gherardi, J. M., Keigwin, L. D. & Brown-Leger, S. Collapse and rapid resumption of Atlantic meridional circulation linked to deglacial climate changes. *Nature* **428**, 834–837 (2004).

66. Sun, Y. et al. Influence of Atlantic meridional overturning circulation on the East Asian winter monsoon. *Nat. Geosci.* **5**, 46–49 (2012).

67. Buizert, C. et al. Greenland temperature response to climate forcing during the last deglaciation. *Science* **345**, 1177–1180 (2014).

68. Parrenin, F. et al. Synchronous change of atmospheric $CO_2$ and Antarctic temperature during the last deglacial warming. *Science* **339**, 1060–1063 (2013).

69. Lu, F., Pausata, F. S. R. & Mohtadi, M. Reconstruct the intertropical convergence zone over the Indo-Pacific Warm Pool with extended records and empirical orthogonal function. *Proc. Natl Acad. Sci. USA* **121**, e2408502121 (2024).

70. Chiang, J. C. H. et al. Role of seasonal transitions and westerly jets in East Asian paleoclimate. *Quat. Sci. Rev.* **108**, 111–129 (2015).

71. Liu, Z. et al. Transient simulation of last deglaciation with a new mechanism for Bølling-Allerød warming. *Science* **325**, 310–314 (2009).

72. Zhao, B. et al. Hydroclimate variation during the mystery interval in the East Asian summer monsoon area. *Quat. Sci. Rev.* **266**, 107075 (2021).

73. Ma, T. et al. Intensified climate drying and cooling during the last glacial culmination (20.8–17.5 cal ka BP) in the south-eastern Asian monsoon domain inferred from a high-resolution pollen record. *Quat. Sci. Rev.* **278**, 107371 (2022).

74. He, C. et al. Deglacial variability of South China hydroclimate heavily contributed by autumn rainfall. *Nat. Commun.* **12**, 5875 (2021).

75. Kageyama, M. et al. Climatic impacts of fresh water hosing under Last Glacial Maximum conditions: a multi-model study. *Climate* **9**, 935–953 (2013).

76. Leng, C. et al. Temperature variability revealed by lacustrine brGDGTs in northeastern China since the Last Glacial Maximum. *Glob. Planet. Change* **234**, 104384 (2024).

77. Xie, S. et al. Concordant monsoon-driven postglacial hydrological changes in peat and stalagmite records and their impacts on prehistoric cultures in central China. *Geology* **41**, 827–830 (2013).

78. Zhang, H. et al. A data-model comparison pinpoints Holocene spatiotemporal pattern of East Asian summer monsoon. *Quat. Sci. Rev.* **261**, 106911 (2021).

79. Li, G. & Xie, S.-P. Tropical biases in CMIP5 multimodel ensemble: the excessive equatorial Pacific cold tongue and double ITCZ problems. *J. Clim.* **27**, 1765–1780 (2014).

80. Kong, W., Swenson, L. M. & Chiang, J. C. H. Seasonal transitions and the westerly jet in the Holocene East Asian summer monsoon. *J. Clim.* **30**, 3343–3365 (2017).

81. Wanner, H. et al. Mid- to late Holocene climate change: an overview. *Quat. Sci. Rev.* **27**, 1791–1828 (2008).

82. Vermeesch, P. IsoplotR: a free and open toolbox for geochronology. *Geosci. Front.* **9**, 1479–1493 (2018).

83. Kröpelin, S. et al. Climate-driven ecosystem succession in the Sahara: the past 6000 years. *Science* **320**, 765–768 (2008).

84. Thompson, L. G. et al. Kilimanjaro ice core records: evidence of Holocene climate change in tropical Africa. *Science* **298**, 589–593 (2002).

85. Pennington, B. T., Hamdan, M. A., Pears, B. R. & Sameh, H. I. Aridification of the Egyptian Sahara 5000-4000cal BP revealed from X-ray fluorescence analysis of Nile Delta sediments at Kom al-Ahmer/Kom Wasit. *Quat. Int.* **514**, 108–118 (2019).

86. Cullen, H. M. et al. Climate change and the collapse of the Akkadian empire: evidence from the deep sea. *Geology* **28**, 379–382 (2000).

87. Carolin, S. A. et al. Precise timing of abrupt increase in dust activity in the Middle East coincident with 4.2 ka social change. *Proc. Natl Acad. Sci. USA* **116**, 67–72 (2019).

88. Bonan, G. B. Forests and climate change: forcings, feedbacks, and the climate benefits of forests. *Science* **320**, 1444–1449 (2008).

89. Pausata, F. S. R. et al. The greening of the Sahara: past changes and future implications. *One Earth* **2**, 235–250 (2020).

90. Marcott, S. A., Shakun, J. D., Clark, P. U. & Mix, A. C. A reconstruction of regional and global temperature for the past 11,300 years. *Science* **339**, 1198–1201 (2013).

91. Hurrell James, W. Decadal trends in the North Atlantic Oscillation: regional temperatures and precipitation. *Science* **269**, 676–679 (1995).

92. Olsen, J., Anderson, N. J. & Knudsen, M. F. Variability of the North Atlantic Oscillation over the past 5,200 years. *Nat. Geosci.* **5**, 808–812 (2012).

93. Ogi, M., Tachibana, Y. & Yamazaki, K. Impact of the wintertime North Atlantic Oscillation on the summertime atmospheric circulation. *Geophys. Res. Lett.* **30**, 1704 (2003).

94. Sung, M.-K. et al. A possible impact of the North Atlantic Oscillation on the East Asian summer monsoon precipitation. *Geophys. Res. Lett.* **33**, L21713 (2006).

95. Chen, T. et al. Radiocarbon evidence for the stability of polar ocean overturning during the Holocene. *Nat. Geosci.* **16**, 631–636 (2023).

96. Hou, J. et al. Large Holocene summer temperature oscillations and impact on the peopling of the northeastern Tibetan Plateau. *Geophys. Res. Lett.* **43**, 1323–1330 (2016).

97. Liu, Y. et al. Land–atmosphere–ocean coupling associated with the Tibetan Plateau and its climate impacts. *Natl Sci. Rev.* **7**, 534–552 (2020).

98. Chandan, D. & Peltier, W. R. African humid period precipitation sustained by robust vegetation, soil, and lake feedbacks. *Geophys. Res. Lett.* **47**, e2020GL088728 (2020).

99. Tabor, C., Otto-Bliesner, B. & Liu, Z. Speleothems of South American and Asian monsoons influenced by a Green Sahara. *Geophys. Res. Lett.* **47**, e2020GL089695 (2020).

100. Tiwari, S. et al. On the remote impacts of mid-Holocene Saharan vegetation on South American hydroclimate: a modeling inter-comparison. *Geophys. Res. Lett.* **50**, e2022GL101974 (2023).

101. Ma, L. *Geological Atlas of China* (Geological Publishing House, 2002).

102. Appleby, P. G. *Chronostratigraphic Techniques in Recent Sediments* (Springer, 2001).

103. Bruel, R. & Sabatier, P. serac: an R package for shortlived radio-nuclide chronology of recent sediment cores. *J. Environ. Radioact.* **225**, 106449 (2020).

104. Grootes, P. M., Nadeau, M.-J. & Rieck, A. $^{14}$C-AMS at the Leibniz-Labor: radiometric dating and isotope research. *Nucl. Instrum. Methods Phys. Res. B Beam Interact. Mater. At.* **223-224**, 55–61 (2004).

105. Wacker, L., Němec, M. & Bourquin, J. A revolutionary graphitisation system: fully automated, compact and simple. *Nucl. Instrum. Methods Phys. Res. B Beam Interact. Mater. At.* **268**, 931–934 (2010).

106. Wacker, L. et al. MICADAS: routine and high-precision radiocarbon dating. *Radiocarbon* **52**, 252–262 (2010).

107. Zhang, H. et al. Testing and assessment of high-precision and high-accuracy AMS-radiocarbon measurements at Nanjing University, China. *Radiocarbon*, 1–12 (2024).

108. Reimer, P. J. et al. The IntCal20 Northern Hemisphere radiocarbon age calibration curve (0-55 cal ka BP). *Radiocarbon* **62**, 725–757 (2020).

109. Hua, Q. et al. Atmospheric radiocarbon for the period 1950-2019. *Radiocarbon* **64**, 723–745 (2022).

110. Ramsey, C. B. & Lee, S. Recent and planned developments of the program OxCal. *Radiocarbon* **55**, 720–730 (2013).

111. Peterson Larry, C., Haug Gerald, H., Hughen Konrad, A. & Röhl, U. Rapid changes in the hydrologic cycle of the tropical Atlantic during the last glacial. *Science* **290**, 1947–1951 (2000).

112. Schulz, H., von Rad, U., Erlenkeuser, H. & von Rad, U. Correlation between Arabian Sea and Greenland climate oscillations of the past 110,000 years. *Nature* **393**, 54–57 (1998).

113. Hughen, K. A., Overpeck, J. T., Peterson, L. C. & Trumbore, S. Rapid climate changes in the tropical Atlantic region during the last deglaciation. *Nature* **380**, 51–54 (1996).

114. Deplazes, G. et al. Links between tropical rainfall and North Atlantic climate during the last glacial period. *Nat. Geosci.* **6**, 213–217 (2013).

115. Ji, J. et al. Asian monsoon oscillations in the northeastern Qinghai-Tibet Plateau since the late glacial as interpreted from visible reflectance of Qinghai Lake sediments. *Earth Planet. Sci. Lett.* **233**, 61–70 (2005).

116. Tjallingii, R., Röhl, U., Kölling, M. & Bickert, T. Influence of the water content on X-ray fluorescence core-scanning measurements in soft marine sediments. *Geochem. Geophys. Geosyst.* **8**, Q02004 (2007).

117. Badgley, G., Field Christopher, B. & Berry Joseph, A. Canopy near-infrared reflectance and terrestrial photosynthesis. *Sci. Adv.* **3**, e1602244 (2017).

118. Weltje, G. J. & Tjallingii, R. Calibration of XRF core scanners for quantitative geochemical logging of sediment cores: theory and application. *Earth Planet. Sci. Lett.* **274**, 423–438 (2008).

119. Didan, K. et al. *Multi-sensor Vegetation Index and Phenology Earth Science Data Records: Algorithm Theoretical Basis Document and User Guide* (The University of Arizona, 2015).

120. Schneider, T. Analysis of incomplete climate data: estimation of mean values and covariance matrices and imputation of missing values. *J. Clim.* **14**, 853–871 (2001).

121. Fierro, R. D., Golub, G. H., Hansen, P. C. & O'Leary, D. P. Regularization by truncated total least squares. *SIAM J. Sci. Comput.* **18**, 1223–1241 (1997).

122. Neukom, R. et al. Inter-hemispheric temperature variability over the past millennium. *Nat. Clim. Change* **4**, 362–367 (2014).

123. Gergis, J., Neukom, R., Gallant, A. J. E. & Karoly, D. J. Australasian temperature reconstructions spanning the last millennium. *J. Clim.* **29**, 5365–5392 (2016).

124. Neukom, R. et al. Consistent multidecadal variability in global temperature reconstructions and simulations over the Common Era. *Nat. Geosci.* **12**, 643–649 (2019).

125. Neukom, R., Steiger, N., Gómez-Navarro, J. J., Wang, J. & Werner, J. P. No evidence for globally coherent warm and cold periods over the preindustrial Common Era. *Nature* **571**, 550–554 (2019).

126. Ahmed, M. et al. Continental-scale temperature variability during the past two millennia. *Nat. Geosci.* **6**, 339–346 (2013).

127. Christiansen, B. & Ljungqvist, F. C. Challenges and perspectives for large-scale temperature reconstructions of the past two millennia. *Rev. Geophys.* **55**, 40–96 (2017).

128. Luterbacher, J., Dietrich, D., Xoplaki, E., Grosjean, M. & Wanner, H. European seasonal and annual temperature variability, trends, and extremes since 1500. *Science* **303**, 1499–1503 (2004).

129. Cook, E. R. et al. Asian monsoon failure and megadrought during the last millennium. *Science* **328**, 486 (2010).

130. Wang, J. et al. Internal and external forcing of multidecadal Atlantic climate variability over the past 1,200 years. *Nat. Geosci.* **10**, 512–517 (2017).

131. Abdi, H. & Williams, L. J. Principal component analysis. *WIREs Comput. Stat.* **2**, 433–459 (2010).

132. Wold, S., Sjöström, M. & Eriksson, L. PLS-regression: a basic tool of chemometrics. *Chemom. Intell. Lab. Syst.* **58**, 109–130 (2001).

133. ter Braak, C. J. F. & Juggins, S. Weighted averaging partial least squares regression (WA-PLS): an improved method for reconstructing environmental variables from species assemblages. *Hydrobiologia* **269**, 485–502 (1993).

134. de Jong, S. SIMPLS: An alternative approach to partial least squares regression. *Chemom. Intell. Lab. Syst.* **18**, 251–263 (1993).

135. van der Voet, H. Comparing the predictive accuracy of models using a simple randomization test. *Chemom. Intell. Lab. Syst.* **25**, 313–323 (1994).

136. Birks, H. Numerical tools in palaeolimnology-progress, potentialities, and problems. *J. Paleolimnol.* **1998**, 307–332 (1998).

137. Christiansen, B. & Ljungqvist, F. C. Reconstruction of the extratropical NH mean temperature over the last millennium with a method that preserves low-frequency variability. *J. Clim.* **24**, 6013–6034 (2011).

138. Tingley, M. P. & Huybers, P. A Bayesian algorithm for reconstructing climate anomalies in space and time. Part I: development and applications to paleoclimate reconstruction problems. *J. Clim.* **23**, 2759–2781 (2010).

139. Blasone, R.-S. et al. Generalized likelihood uncertainty estimation (GLUE) using adaptive Markov Chain Monte Carlo sampling. *Adv. Water Resour.* **31**, 630–648 (2008).

140. Wang, Z. et al. Human-induced erosion has offset one-third of carbon emissions from land cover change. *Nat. Clim. Change* **7**, 345–349 (2017).

141. Shi, F. et al. Interdecadal to multidecadal variability of East Asian summer monsoon over the past half millennium. *J. Geophys. Res. Atmos.* **127**, e2022JD037260 (2022).

142. Hastings, W. K. Monte Carlo sampling methods using Markov chains and their applications. *Biometrika* **57**, 97–109 (1970).

143. Shi, F. et al. The position of the current warm period in the context of the past 22,000 years of summer climate in China. *Geophys. Res. Lett.* **48**, e2020GL091940 (2021).

144. Marvel, K. et al. Twentieth-century hydroclimate changes consistent with human influence. *Nature* **569**, 59–65 (2019).

145. Hoerl, A. E. & Kennard, R. W. Ridge regression: biased estimation for nonorthogonal problems. *Technometrics* **12**, 55–67 (1970).

146. Tibshirani, R. Regression shrinkage and selection via the lasso. *J. R. Stat. Soc. B* **58**, 267–288 (1996).

147. Zou, H. & Hastie, T. Regularization and variable selection via the elastic net. *J. R. Stat. Soc. B Stat. Methodol.* **67**, 301–320 (2005).

148. Sun, Z. et al. A review of Earth artificial intelligence. *Comput. Geosci.* **159**, 105034 (2022).

149. Reichstein, M. et al. Deep learning and process understanding for data-driven Earth system science. *Nature* **566**, 195–204 (2019).

150. LeCun, Y., Bengio, Y. & Hinton, G. Deep learning. *Nature* **521**, 436–444 (2015).

151. Wunsch, A., Liesch, T. & Broda, S. Deep learning shows declining groundwater levels in Germany until 2100 due to climate change. *Nat. Commun.* **13**, 1221 (2022).

152. Ioffe, S. & Szegedy, C. Batch normalization: accelerating deep network training by reducing internal covariate shift. *Proc. 32nd Int. Conf. Mach. Learn.* **37**, 448–456 (2015).

153. Srivastava, N., Hinton, G., Krizhevsky, A., Sutskever, I. & Salakhutdinov, R. Dropout: a simple way to prevent neural networks from overfitting. *J. Mach. Learn. Res.* **15**, 1929–1958 (2014).

154. He, K., Zhang, X., Ren, S. & Sun, J. Delving deep into rectifiers: surpassing human-level performance on ImageNet classification. In *2015 IEEE International Conference on Computer Vision* 1026–1034 (IEEE, 2015).

155. Salamon, J. & Bello, J. P. Deep convolutional neural networks and data augmentation for environmental sound classification. *IEEE Signal Process. Lett.* **24**, 279–283 (2017).

156. Lu, F., Mohtadi, M. & Pausata, F. S. R. Dynamics of the intertropical convergence zone during the early Heinrich Stadial 1. *Nat. Commun.* **15**, 9753 (2024).

157. Blaauw, M. & Christen, J. A. Flexible paleoclimate age-depth models using an autoregressive gamma process. *Bayesian Anal.* **6**, 457–474 (2011).

158. Bintanja, R., van de Wal, R. S. W. & Oerlemans, J. Modelled atmospheric temperatures and global sea levels over the past million years. *Nature* **437**, 125–128 (2005).

159. Berger, A. Long-term variations of daily insolation and Quaternary climatic changes. *J. Atmos. Sci.* **35**, 2362–2367 (1978).

160. Joos, F. & Spahni, R. Rates of change in natural and anthropogenic radiative forcing over the past 20,000 years. *Proc. Natl Acad. Sci. USA* **105**, 1425 (2008).

161. Peltier, W. R. Global glacial isostasy and the surface of the ice-age Earth: the ICE-5G (VM2) model and grace. *Annu. Rev. Earth Planet. Sci.* **32**, 111–149 (2004).

162. Brady, E. et al. The connected isotopic water cycle in the Community Earth System Model version 1. *J. Adv. Model. Earth Syst.* **11**, 2547–2566 (2019).

163. Peltier, W. R., Argus, D. F. & Drummond, R. Space geodesy constrains ice age terminal deglaciation: the global ICE-6G_C (VM5a) model. *J. Geophys. Res. Solid Earth* **120**, 450–487 (2015).

164. Hazeleger, W. et al. EC-Earth: a seamless Earth-system prediction approach in action. *Bull. Am. Meteorol. Soc.* **91**, 1357–1364 (2010).

165. Döscher, R. et al. The EC-Earth3 Earth system model for the Coupled Model Intercomparison Project 6. *Geosci. Model Dev.* **15**, 2973–3020 (2022).

166. Zhang, Q. et al. Simulating the mid-Holocene, last interglacial and mid-Pliocene climate with EC-Earth3-LR. *Geosci. Model Dev.* **14**, 1147–1169 (2021).

167. Bosmans, J. H. C. et al. Monsoonal response to mid-Holocene orbital forcing in a high resolution GCM. *Clim. Past* **8**, 723–740 (2012).

168. Braconnot, P. et al. Evaluation of climate models using palaeoclimatic data. *Nat. Clim. Change* **2**, 417–424 (2012).

169. Berger, A. Long-term variations of caloric insolation resulting from the Earth's orbital elements. *Quat. Res.* **9**, 139–167 (1978).

170. McGee, D., deMenocal, P. B., Winckler, G., Stuut, J. B. W. & Bradtmiller, L. I. The magnitude, timing and abruptness of changes in North African dust deposition over the last 20,000 yr. *Earth Planet. Sci. Lett.* **371-372**, 163–176 (2013).

## Author contributions
H.L. and F.L. conceived and designed the study. H.L. and S.Y. organized core drilling. F.L., F.Y. and X.D. split the cores and prepared the samples. Y.G., P.L. and F.L. performed AMS ^{14}C dating supervised by H.Z. F.L. performed ^{210}Pb and ^{137}Cs dating, proxy measurements, rainfall reconstructions, Bayesian age modeling, and statistical analyses. Q.Z. ran the Green Sahara experiments. Z.L. downloaded and preprocessed the iTRACE and TRACE-21ka data. Z.L. and F.L. analyzed the model results. F.L. and H.L. wrote and revised the manuscript, P.L., Z.L., Q.Z., S.Y., D.C., F.S.R.P., M.B.-Y. and J.V.M. discussed and contributed to the revision of the manuscript.

## Competing interests
The authors declare no competing interests.

## Additional information
**Supplementary information** The online version contains supplementary material available at https://doi.org/10.1038/s41467-025-55888-w.

**Correspondence** and requests for materials should be addressed to Huayu Lu.

**Peer review information** *Nature Communications* thanks Jean-Philippe Baudouin, Jule Xiao and the other, anonymous, reviewer(s) for their contribution to the peer review of this work. A peer review file is available.

**Reprints and permissions information** is available at http://www.nature.com/reprints